

# Global Biogeochemical Cycles®



## RESEARCH ARTICLE

10.1029/2022GB007677

## Recent Trends and Variability in the Oceanic Storage of Dissolved Inorganic Carbon

L. Keppler<sup>1,2,3</sup> , P. Landschützer<sup>2,4</sup>, S. K. Lauvset<sup>5</sup> , and N. Gruber<sup>6</sup> 

<sup>1</sup>Scripps Institution of Oceanography, University of California San Diego, La Jolla, CA, USA, <sup>2</sup>Max Planck Institute for Meteorology, Hamburg, Germany, <sup>3</sup>International Max Planck Research School on Earth System Modelling, Hamburg, Germany, <sup>4</sup>Flanders Marine Institute (VLIZ), Ostend, Belgium, <sup>5</sup>NORCE Norwegian Research Centre, Bjerknes Centre for Climate Research, Bergen, Norway, <sup>6</sup>Environmental Physics, Institute of Biogeochemistry and Pollutant Dynamics, ETH Zurich, Zurich, Switzerland

### Key Points:

- From 2004 through 2019, the global oceanic dissolved inorganic carbon (DIC) pool increased at an average rate of  $3.2 \pm 0.7$  Pg C yr<sup>-1</sup>
- Most of this increase is associated with the uptake of anthropogenic CO<sub>2</sub>, while natural CO<sub>2</sub> is mostly redistributed within the ocean
- The interannual variability of DIC is largest in the tropical Pacific Ocean

### Supporting Information:

Supporting Information may be found in the online version of this article.

### Correspondence to:

L. Keppler,  
lkeppler@ucsd.edu

### Citation:

Keppler, L., Landschützer, P., Lauvset, S. K., & Gruber, N. (2023). Recent trends and variability in the oceanic storage of dissolved inorganic carbon. *Global Biogeochemical Cycles*, 37, e2022GB007677. <https://doi.org/10.1029/2022GB007677>

Received 19 DEC 2022

Accepted 7 APR 2023

**Abstract** Several methods have been developed to quantify the oceanic accumulation of anthropogenic carbon dioxide (CO<sub>2</sub>) in response to rising atmospheric CO<sub>2</sub>. Yet, we still lack a corresponding estimate of the changes in the total oceanic dissolved inorganic carbon (DIC). In addition to the increase in anthropogenic CO<sub>2</sub>, changes in DIC also include alterations of natural CO<sub>2</sub>. Once integrated globally, changes in DIC reflect the net oceanic sink for atmospheric CO<sub>2</sub>, complementary to estimates of the air-sea CO<sub>2</sub> exchange based on surface measurements. Here, we extend the MOBO-DIC machine learning approach by Keppler et al. (2020a, <https://www.ncei.noaa.gov/access/metadata/landing-page/bin/iso?id=gov.noaa.nodc%3A0221526>) to estimate global monthly fields of DIC at 1° resolution over the top 1,500 m from 2004 through 2019. We find that over these 16 years and extrapolated to cover the whole global ocean down to 4,000 m, the oceanic DIC pool increased close to linearly at an average rate of  $3.2 \pm 0.7$  Pg C yr<sup>-1</sup>. This trend is statistically indistinguishable from current estimates of the oceanic uptake of anthropogenic CO<sub>2</sub> over the same period. Thus, our study implies no detectable net loss or gain of natural CO<sub>2</sub> by the ocean, albeit the large uncertainties could be masking it. Our reconstructions suggest substantial internal redistributions of natural oceanic CO<sub>2</sub>, with a shift from the midlatitudes to the tropics and from the surface to below ~200 m. Such redistributions correspond with the Pacific Decadal Oscillation and the Atlantic Multidecadal Oscillation. The interannual variability of DIC is strongest in the tropical Western Pacific, consistent with the El Niño Southern Oscillation.

**Plain Language Summary** Human activities, such as the burning of fossil fuels, increase the amount of the greenhouse gas carbon dioxide (CO<sub>2</sub>) in the atmosphere. A large portion of this additional CO<sub>2</sub> is being taken up by the ocean. Several methods have been developed to quantify how much of this anthropogenic CO<sub>2</sub> is taken up by the ocean. However, in addition to the anthropogenic CO<sub>2</sub>, there can also be changes in the naturally occurring CO<sub>2</sub> in the ocean. Both the anthropogenic and the natural changes would be reflected in changes of the total dissolved inorganic carbon (DIC) stored in the ocean. Here, we extend a machine learning approach to estimate global monthly fields of DIC from 2004 through 2019. We find that over these 16 years, the oceanic DIC pool in the upper 4,000 m increased at an average rate of  $3.2 \pm 0.7$  Pg C/yr. This trend is statistically indistinguishable from current estimates of the oceanic uptake of anthropogenic CO<sub>2</sub> over the same period. Thus, our study implies no detectable net loss or gain of natural CO<sub>2</sub> by the ocean, albeit the large uncertainties could be masking it. Our reconstructions suggest substantial internal redistributions of natural oceanic CO<sub>2</sub>.

## 1. Introduction

The global oceanic dissolved inorganic carbon (DIC) pool is a powerful recorder of changes in the net exchange of carbon dioxide (CO<sub>2</sub>) across the air-sea interface, that is, the strength of the net oceanic carbon sink. This net sink is the sum of a flux of natural carbon ( $C_{nat}$ ) that reflects the exchange driven by changes in solubility, ocean circulation, mixing, and biological processes, and the flux of anthropogenic carbon ( $C_{am}$ ) that corresponds to the anomalous flux of CO<sub>2</sub> driven by the human-induced rise in atmospheric CO<sub>2</sub> (Gruber et al., 2023; McNeil & Matear, 2013). When integrated globally, the sources and sinks of natural CO<sub>2</sub> fluxes cancel each other out in a steady state as the ocean strives toward equilibrium with the overlaying atmosphere (Landschützer et al., 2022). On the contrary, the observed increase in the net air-sea CO<sub>2</sub> exchange is caused by anthropogenic CO<sub>2</sub> emissions (Friedlingstein et al., 2022). An important exception is residual outgassing that reflects the balance between

© 2023. The Authors.

This is an open access article under the terms of the Creative Commons Attribution-NonCommercial-NoDerivs License, which permits use and distribution in any medium, provided the original work is properly cited, the use is non-commercial and no modifications or adaptations are made.

the input of carbon by rivers and the deposition of carbon on the seafloor (Regnier et al., 2022; Sarmiento & Sundquist, 1992). As long as this balance is maintained, this latter (i.e., natural) component does not leave an imprint on changes in DIC, so that changes in this pool are then directly attributable to the ocean interior accumulation or loss of both natural and anthropogenic CO<sub>2</sub>.

Knowing the magnitude of the net oceanic sink for CO<sub>2</sub> is crucial for closing the global carbon budget and its anthropogenic perturbation (Friedlingstein et al., 2022; Sarmiento & Gruber, 2002). The need is heightened by efforts such as the United Nations' global stocktake efforts (<https://unfccc.int/topics/science/workstreams/global-stocktake>), which require a more refined estimate of the changing ocean carbon content, connecting the surface and interior ocean, and demonstrating the total changes in DIC, as well as its spatial distribution. Finally, better global-scale constraints on the changes in oceanic DIC are of great interest to better document the progression of ocean acidification and better establish the connection between changes in seawater chemistry and biological impacts (Doney et al., 2009; Feely et al., 2004; Orr et al., 2005).

In terms of observations, the net oceanic CO<sub>2</sub> sink is at present primarily determined using measurements of the surface ocean partial pressure of CO<sub>2</sub> (pCO<sub>2</sub>), which are mapped to the globe using various data interpolation methods (Fay et al., 2021; Gregor & Gruber, 2021; Landschützer et al., 2014; Rödenbeck et al., 2015). The mapped pCO<sub>2</sub> is then used, in combination with the atmospheric pCO<sub>2</sub> and the gas transfer velocity to estimate the air-sea CO<sub>2</sub> flux. However, this approach is subject to various uncertainties, such as data sparsity (Fay & McKinley, 2013), an ill-constrained gas transfer coefficient (Roobaert et al., 2019; Wanninkhof et al., 2009), and a potential offset in the pCO<sub>2</sub> measurements as they are not directly taken at the cool skin surface (Watson et al., 2020). Furthermore, the steady-state outgassing of river-derived carbon needs to be subtracted from the inferred flux to obtain the anthropogenic flux relevant to the global carbon budget. Estimates for this riverine flux range from 0.23 Pg C yr<sup>-1</sup> (Lacroix et al., 2020) and 0.45 ± 0.18 Pg C yr<sup>-1</sup> (Jacobson et al., 2007) to 0.78 ± 0.41 Pg C yr<sup>-1</sup> (Resplandy et al., 2018), with the most recent review by Regnier et al. (2022) suggesting a value of 0.65 ± 0.3 Pg C yr<sup>-1</sup>. This range and the associated uncertainties add further uncertainty to the pCO<sub>2</sub> derived estimates of the net carbon uptake by the global ocean.

Confidence in quantifying this net uptake could be strengthened if constrained independently through the direct determination of changes in the global ocean DIC content. Nevertheless, this is a challenging task, owing to the sparsity of observations, the substantial background DIC pool of ~37,000 Pg C (Kepler et al., 2020b), and the many physical and biological processes that govern the distribution of DIC in the ocean (Sarmiento & Gruber, 2006). A very successful approach to overcome this challenge has been to only focus on the interior ocean's accumulation of the C<sub>ant</sub> component (Tanhua et al., 2007; Wallace, 1995). Under the assumption that the ocean is in a near steady state, several methods have been developed to determine the changes in C<sub>ant</sub> either from single surveys of DIC (Brewer, 1978; Chen & Millero, 1979; Gruber et al., 1996) or from repeat hydrography programs (Carter et al., 2019; Clement & Gruber, 2018; Friis et al., 2005). The application of these methods has permitted the oceanographic community to quantify the increase in the C<sub>ant</sub> inventory, both since preindustrial times (Gruber, 1998; Sabine et al., 1999) and for the past few decades (Carter et al., 2019; Friis et al., 2005; Wanninkhof et al., 2010), with the global studies providing invaluable constraints for the global budget of C<sub>ant</sub> (Gruber et al., 2019; Sabine et al., 2004).

Although these global C<sub>ant</sub> estimates have proven to be extremely valuable for constraining the global carbon budget and hence the fate of the emitted anthropogenic CO<sub>2</sub>, they have not been able to fully address whether the steady-state assumption or the assumption of a small C<sub>nat</sub> signal is justified. Questions were raised early on, especially in the context of ocean warming (Keeling, 2005; Sabine & Gruber, 2005), which many models suggest will lead to a loss of CO<sub>2</sub> from the ocean (Joos et al., 1999; Matear & Hirst, 1999; Sarmiento et al., 1998). Later, using a combination of different model and observation-based methods, McNeil and Matear (2013) invoked the presence of a decadal-scale outgassing signal of C<sub>nat</sub>, but without being able to support this conjecture with direct observations. Dedicated modeling studies also suggest that the ocean might have lost C<sub>nat</sub> in recent decades, for example, in response to the trends in the Southern Annular Mode (Hauck et al., 2013; Lenton & Matear, 2007; Le Quéré et al., 2007; Lovenduski et al., 2007, 2008; Zickfeld et al., 2007). In their global study on the increase in anthropogenic CO<sub>2</sub> between 1994 and 2007, Gruber et al. (2019) speculated that perhaps as much as 5 Pg C of C<sub>nat</sub> might have been lost from the ocean over this period. A recent review by Gruber et al. (2023) further assessed the role of the nonsteady state and the associated potential loss of C<sub>nat</sub>. Conversely, enhanced lateral transport of natural carbon from the land could yield a gain of C<sub>nat</sub> in the ocean (Regnier et al., 2022). Similarly, changes in the

circulation or biological productivity could cause an anomalous uptake or release of CO<sub>2</sub> from the atmosphere, altering the total stock of C<sub>nat</sub>.

As the arguments for potential changes in C<sub>nat</sub> accumulate, the need to constrain the changes in the total DIC pool increases, as this permits to assess the changes in both natural and anthropogenic CO<sub>2</sub>. When doing so, one needs to also consider that even if the global-scale changes in the natural CO<sub>2</sub> pool might be small, this pool is subject to strong redistributions within the ocean, associated with changes in circulation, shifts in ocean fronts, and changes in biological productivity, causing locally large changes in DIC (Clement & Gruber, 2018). Such changes are commonly seen when comparing the DIC distributions between two occupations of a particular hydrographic section (Carter et al., 2019; Wanninkhof et al., 2010). They are also expected in the context of interannual variability, especially in regions with large vertical undulations of the thermocline, and hence also the “carbocline,” that is, the strong vertical gradient in DIC. Such redistributions of DIC within the ocean not only pose a challenge for the detection of global-scale changes in the DIC pool, but they also potentially threaten organisms, as spatial redistributions of DIC might cause more rapid local changes in ocean acidification and, perhaps, a more rapid reaching of critical thresholds (McNeil & Sasse, 2016).

Currently, no sensor technology exists that can operationally measure DIC in situ. Thus, we must rely on physical seawater samples collected and analyzed during ship-based surveys and programs (Bates et al., 2014; Talley et al., 2016), strongly limiting the coverage and the sampling frequency. Most of these DIC measurements and the associated ancillary data are compiled and subjected to secondary quality control by the Global Ocean Data Analysis Project (GLODAP; Key et al., 2004; Olsen et al., 2016). A recent version (GLODAPv2.2021) contains over 1 million measurements from across the global ocean, spanning measurements from 1972 to 2020 (Lauvset et al., 2021). Most of the measurements contained within GLODAP stem from repeat hydrography programs, where the same set of stations along long lines are revisited at roughly decadal intervals (Talley et al., 2016). In addition to GLODAP, some long-term time series stations provide information on the temporal variability in the interior ocean at a few locations, including the Hawaii Ocean Time series (HOT; Dore et al., 2009) and the Bermuda Atlantic Time series Study (BATS; Bates et al., 2014). More recently, Argo floats equipped with biogeochemical (BGC) sensors that measure pH, salinity, and other variables supplement the ship data. Using these float measurements and some empirical relationships to infer alkalinity, DIC can be estimated (Carter et al., 2018; van Heuven et al., 2011). However, this method has much larger uncertainties than the ship data (Bittig et al., 2018), and to date, the available BGC-Argo float data are largely limited to the Southern Ocean, as part of the Southern Ocean Carbon and Climate Observations and Modeling project (SOCCOM; Talley et al., 2019), while the global ocean BGC-Argo array is still in its early stages (Bittig et al., 2019).

In parallel to the efforts in combining and unifying carbon cycle observations (Bakker et al., 2016; Olsen et al., 2016), a second branch related to big data analysis based on machine learning has emerged. Keppler et al. (2020b) adopted a cluster-regression approach previously applied to reconstruct the air-sea CO<sub>2</sub> exchange (Landschützer et al., 2013, 2014) and extended it to map a monthly climatology of DIC in the upper 2,000 m of the near-global ocean, that is, Mapped Observation-Based Oceanic DIC (MOBO-DIC; Keppler et al., 2020a). Similarly, Broullón et al. (2020) developed a single-step machine learning approach to map the monthly climatology of interior DIC at a global scale. In addition, a recent study has mapped out the temporal evolution of DIC globally (Gregor & Gruber, 2021), but this approach was limited to the documentation of variations at the sea surface. These studies revealed the feasibility of reconstructing the DIC content from observations at the global scale. In addition, using CMIP6 models and synthetic Argo data, Turner et al. (2022) demonstrated very recently that interior temperature and salinity data are well suited to reconstruct interior DIC fields and their variability. However, they have not yet mapped the interior ocean DIC with real-world Argo observations. Further, Sharp et al. (2022) successfully mapped monthly fields of interior ocean dissolved oxygen at a global scale, using a machine learning approach. However, mapped estimates of interior observation-based DIC remain limited to seasonal climatologies (Broullón et al., 2020; Keppler et al., 2020b) or the surface (Gregor & Gruber, 2021), and reconstructions of the trend and interannual variability of the upper ocean total DIC at the global scale based on direct observations are still lacking.

To fill this gap, we use the MOBO-DIC approach and extend the monthly climatology of DIC by Keppler et al. (2020b) to resolve monthly global DIC fields from 2004 through 2019 (i.e., January 2004 through December 2019). The temporal extent of our reconstructions is primarily determined by the availability of temperature and salinity fields from the Argo program that we use as key predictors. Our new DIC product is mapped at a

monthly resolution on a  $1^\circ \times 1^\circ$  grid, from  $65^\circ\text{N}$  to  $65^\circ\text{S}$ , and reaching  $80^\circ\text{N}$  in the Atlantic (see Figure S1 in Supporting Information S1), extending from 2.5 to 1,500 m depth. Subsequently, we investigate the trend and interannual variability of the interior oceanic DIC at a global scale and put these changes into the context of the ongoing accumulation of anthropogenic  $\text{CO}_2$  in the ocean's interior and from this, infer the changes in the natural  $\text{CO}_2$  pool.

## 2. Data and Methods

### 2.1. Cluster-Regression

We adopt the two-step neural network MOBO-DIC approach introduced by Keppler et al. (2020b) to map the sparse DIC observations to the (near) global ocean at monthly resolution for the period January 2004 through December 2019. Here, we present a summary of the most important features and the main changes compared to the climatological approach taken by Keppler et al. (2020b). Our approach first clusters the ocean into regions of similar properties using self-organizing maps (SOM) and then applies a feed-forward neural network (FFN) in each cluster to reconstruct a physical relationship between a set of driver variables and the target DIC data. This cluster-regression approach does not require information about the measurement location, a feature that separates it from many other mapping approaches (Bittig et al., 2018; Broullón et al., 2019, 2020; Gregor et al., 2017; Sasse et al., 2013). Thus, our regression method is solely based on the physical and biogeochemical relations between the predictor and target variables. Not using the measurement location as a predictor permits our method to benefit from information obtained in other places within each cluster, where predictor and target data are similarly related. Due to data availability (silicic acid and nitrate are only available in the upper 500 m) and the presence of different processes near the surface and below, we run the method separately for two depth slabs: from 2.5 to 500 m and from 500 to 1,500 m. We take the mean of the two estimates at 500 m to minimize boundary problems between the two depth slabs. This approach does not eliminate all discontinuities, but they are well within the uncertainty limits of the method.

In the first step, we use a SOM, that is, a type of unsupervised machine learning, to determine clusters. Following Keppler et al. (2020b), we use six clusters in the upper 500 m and four between 500 and 1,500 m. We tested various set-ups, including different numbers of clusters and found that this number of clusters leads to the smallest overall error in the DIC reconstruction. To avoid boundary problems inherent in cluster-regression approaches, we adjust the original method by creating an ensemble of SOM clusters, following the approach introduced by Gregor and Gruber (2021). To this end, we performed the SOM-step three times, where the DIC input has a different weight ranging from 2 to 4 in each run. The resulting SOM clusters vary mostly around the boundaries (see Figure S2 in Supporting Information S1). In the second step, we run an FFN for each SOM cluster. Our FFN network architecture consists of 8 neurons in the hidden layer of the FFN, as this setup results in the most robust output based on a comparison between the mapped output and the original training data.

To avoid overfitting, we use 80% of the input data to train the network and the remaining 20% for internal cross-validation. As the training and validation data are separated randomly, the output from the FFN is slightly different each time it is run. For each SOM setup, we run the FFN five times, where each time, the data are separated differently into training and validation data to create an ensemble of outputs. Thus, our ensemble comprises 15 members (three SOM setups, each with five FFN runs). The final reported data are the mean across the ensemble, and the standard deviation across the ensemble represents the uncertainty linked to the weighting of the SOM clusters and the random assignment of training and validation data (hereafter referred to as prediction uncertainty, see Figure S3 in Supporting Information S1). We smooth the ensemble mean fields at each depth level by taking the running mean with a window size of three grid cells in each horizontal direction (latitude and longitude) and the temporal dimension.

Some runs produced outputs with unlikely values, for example, considerably larger or smaller than the measured variables in GLODAP. We attribute this to the random assignment of training and validation data, where some data subsets are unsuitable for training. Such runs with unlikely values occurred both with the GLODAP training data and with synthetic data, so it cannot be attributed to noise in the observations. We have tried many different setups of the network to eliminate this issue. However, with the current training data, we were unable to resolve it. Thus, when an output results in values that are more than five standard deviations larger or smaller than the observed data in GLODAP (i.e., outside of the range  $1,639\text{--}2,575 \mu\text{mol kg}^{-1}$  and  $1,898\text{--}2,629 \mu\text{mol kg}^{-1}$  for the upper and lower depth slab, respectively), the entire ensemble member was discarded and rerun with the

same setup but with a different sub-set of training data. We trust that removing the runs with unlikely values, in addition to the bootstrapping approach, yields a robust estimate.

## 2.2. Data and Domain

As input to the SOM, we use monthly mapped fields of temperature and salinity based on Argo float measurements (Roemmich & Gilson, 2009) and an annual-mean climatology of DIC (Lauvset et al., 2016). We weigh the DIC input stronger than the physical predictors so that the clusters largely represent the climatological mean DIC and, to a lesser extent, the physical water masses, following Landschützer et al. (2013).

For the FFN step, we use the ship measurements of DIC from GLODAPv2.2021 between January 2004 and December 2019 (Lauvset et al., 2021) as the target data. We only retain GLODAP data with a WOCE quality control of 0 or 2 and a secondary quality control flag of 1. As predictors, we use the same Argo-based temperature and salinity fields that we used during the SOM step. In addition, we use monthly climatologies of mapped dissolved oxygen, nitrate, and silicic acid from the World Ocean Atlas 2018 (WOA18; Boyer et al., 2018). These climatologies are based on ship measurements from 1955 through 2017 and were interpolated to the global ocean using optimal interpolation. As the nitrate and silicic acid from WOA only extend until 500 m, they were not used as predictors in the deeper slab, while dissolved oxygen extends to 1,500 m in WOA and is thus a predictor variable in both depth slabs. Deviating from the approach taken to produce the monthly climatology of MOBO-DIC (Keppler et al., 2020b), we use atmospheric  $p\text{CO}_2$  as an additional predictor in the upper depth slab (0–500 m) to be able to represent the long-term trend in the atmospheric  $\text{CO}_2$  concentration. Atmospheric  $p\text{CO}_2$  at each grid cell was computed from the GlobalView marine boundary layer product of the mole fraction of  $\text{CO}_2$  ( $x\text{CO}_2$ ; GlobalView-CO<sub>2</sub>, 2011) and converted to  $p\text{CO}_2$  following Landschützer et al. (2013). In the deeper slab below 500 m, we use Julian days as a predictor to represent any long-term trend in the data. We tested various set-ups where we use latitude and longitude (in the form of  $\sin(\text{lon})$  and  $\cos(\text{lon})$ ), and depth as input variables, and found that the inclusion of this spatial information in the predictors did not improve our DIC reconstructions. Thus, the predictors between the surface and 500 m are temperature, salinity, dissolved oxygen, nitrate, silicic acid, and atmospheric  $p\text{CO}_2$ . Between 500 and 1,500 m, we use temperature, salinity, dissolved oxygen, and Julian day as predictors. A more detailed discussion on the choice of predictors can be found in Keppler et al. (2020b).

Note that we use the mapped monthly mean fields as predictors, as opposed to the comeasured data from GLODAP during the training step of the FFN. We tested both approaches but found the results were very noisy when using the comeasured data as predictors. This noisy output may be partially caused by the WOA monthly gridded fields being smoother than the point measurements in GLODAP. Furthermore, using the comeasured predictors leads to a substantial loss of training data, as in  $\sim 60,000$  data points out of  $\sim 440,000$  (i.e.,  $\sim 14\%$ ), the training data do not have usable comeasured predictors.

The availability of the data limits the domain and resolution of our mapping approach. For example, we limit the vertical extent of the multiyear product here to 1,500 m (as opposed to 2,000 m used for the MOBO-DIC climatology) as the DIC observations are very sparse below 1,500 m and only temperature and salinity are available as physical or biogeochemical predictors there. This lack of predictors below 1,500 m prevents a robust estimate of the DIC variations and trends at these depths. Temporally and spatially, the limits tend to be set by the predictor data. The Argo-based data products used here extend from  $65^\circ\text{N}$  to  $65^\circ\text{S}$  globally, to  $80^\circ\text{N}$  in the Atlantic Ocean, with shallow coastal regions being masked, marking the horizontal extent of our domain. As the mapped Argo-data set starts in 2004, and GLODAPv2.2021 includes cruise data until January 2020, the temporal extent of MOBO-DIC is from January 2004 through December 2019.

All predictors have a monthly resolution on  $1^\circ \times 1^\circ$  grids, and we interpolate them onto 28 uneven depth levels between 2.5 and 1,500 m. Note that due to an update to the Argo data, the domain of this study is slightly larger than in the monthly climatology of MOBO-DIC (Keppler et al., 2020b): it extends further north in the Atlantic (until  $80^\circ\text{N}$  instead of  $65^\circ\text{N}$ ), and some more coastal and shallow regions are included (see Figure S1 in Supporting Information S1). As the domain covers most of the global ocean, we refer to our domain as global in-text but want to note that it is technically only near-global.

## 2.3. Calculation of the Trend and Inventory Changes

We estimate the trend in DIC over our period based on the slope of a linear regression of the deseasonalized DIC at each grid cell. The data were deseasonalized by applying a 12-month running mean at each grid cell.

To calculate the trends in the inventories, we first normalize DIC for salinity (hereafter sDIC) to remove any effects from potential changes in the salinity, following Friis et al. (2003). For this normalization, we use the same monthly Argo-based salinity product as above (Roemmich & Gilson, 2009), using the temporal mean salinity from 2004 through 2019 at each grid cell as reference salinity. We convert sDIC from gravimetric (unit:  $\mu\text{mol kg}^{-1}$ ) to volumetric (unit:  $\mu\text{mol m}^{-3}$ ), and then vertically integrate the volumetric trend in the whole domain (upper 1,500 m). To estimate the uncertainty in the trend, we calculate it with each of the 15 ensemble members and take the standard deviation range as the uncertainty range. Note that the uncertainty of the trend only includes the ensemble spread (i.e., the prediction uncertainty) and does not consider other sources of error, for example, those associated with measurements or representation uncertainty. We trust that there should not be a trend in measurement or representation uncertainty in the data, yielding a robust estimate of the overall trend uncertainty. We then conduct an upscaling to estimate the global changes in sDIC that include regions beyond our domain, that is, the high latitudes, coastal regions, and below 1,500 m (see Text S3 in Supporting Information S1).

#### 2.4. Comparison With $C_{ant}$

We compare the trend in MOBO-DIC with an estimate of the change in anthropogenic  $\text{CO}_2$  ( $\Delta C_{ant}$ ). For this comparison, we use two estimates of  $C_{ant}$  and scale them to our study period. The two estimates are (a) the total change in  $C_{ant}$  between 1800 and 2007 and (b) the change in  $C_{ant}$  between 1994 and 2007. The former is estimated by adding the total  $C_{ant}$  up to 1994 estimated by Sabine et al. (2004) to the change in  $C_{ant}$  between 1994 and 2007 estimated by Gruber et al. (2019). For the latter, we use the  $\Delta C_{ant}$  by Gruber et al. (2019).

To scale  $C_{ant}$  to our period, we apply the transient steady-state approach described by Mikaloff Fletcher et al. (2006) and Gruber et al. (2019), which relies on the assumption that the change in  $C_{ant}$  scales with the change in atmospheric  $\text{CO}_2$ :

$$\Delta C_{ant}^{t_3-t_2} = \alpha(t_0, t_1, t_2, t_3) \cdot \Delta C_{ant}^{t_1-t_0} \quad (1)$$

where  $t_0$  and  $t_1$  are the bounds of the periods used to determine  $\Delta C_{ant}$  (either 1800 through 2006 or 1994 through 2006) and  $t_2$  and  $t_3$  bound the period to which the scaling should be applied to (here: 2004 through 2019). The scaling factor  $\alpha$  is specific for each pair of periods, that is, is a function of  $t_0$ ,  $t_1$ ,  $t_2$ , and  $t_3$  and can be estimated from the relative changes in atmospheric  $\text{CO}_2$ , also considering changes in the Revelle factor (Sarmiento et al., 1995) and the changes in the air-sea disequilibrium (Gruber et al., 1996; Matsumoto & Gruber, 2005):

$$\alpha(t_0, t_1, t_2, t_3) = \frac{\Delta_r pCO_2^{atm}(t_3 - t_2)}{\Delta_r pCO_2^{atm}(t_1 - t_0)} \cdot \frac{\xi(t_2..t_3)}{\xi(t_0..t_1)} \cdot \frac{\gamma(t_2..t_3)}{\gamma(t_0..t_1)} \quad (2)$$

where the first factor on the right-hand side is the relative change in atmospheric  $\text{CO}_2$ , the second factor is the relative change in the disequilibrium  $\xi$ , and the third factor is the relative change in the Revelle factor  $\gamma$ .

In the first case, that is, for the base period 1800 through 2006, inserting the observed values in atmospheric  $\text{CO}_2$  in the respective years ( $t_0 = 1800$ , 280 ppm;  $t_1 = 2006$ , 381 ppm;  $t_2 = 2004$ , 377 ppm;  $t_3 = 2019$ , 410 ppm) gives a value of 0.33 for the first factor on the right-hand side of Equation 2. For the disequilibrium, we take the same estimate Gruber et al. (2019) used when scaling from 1800 through 1993 to 1994 through 2006. They estimated a change in the disequilibrium of about 6  $\mu\text{atm}$  between 1800 and 1994 and about 3  $\mu\text{atm}$  between 1994 and 2007, yielding a ratio of 0.94. Similarly, we also take the estimate by Gruber et al. (2019) of 0.94 for the third factor, that is, the ratio of the Revelle factors. Entering these three ratios, we obtain an overall scaling factor  $\alpha$  of 0.29 ( $0.33 \cdot 0.94 \cdot 0.94$ ) when comparing the period 1800 to 2007 with the period from 2004 through 2019.

In the second case, the base period for the scaling factor goes from 1994 ( $t_0$ , 358 ppm) through 2006 ( $t_1$ , 381 ppm), yielding a relative change in atmospheric  $\text{CO}_2$  of 1.45 compared to the period 2004 ( $t_2$ , 377 ppm) through 2019 ( $t_3$ , 410 ppm). As the two periods are largely overlapping in this case, we assume that the ratio of the disequilibrium and the ratio of the Revelle factors are very close to 1 and thus set their values to 1, yielding an overall scaling factor  $\alpha$  of 1.45 when comparing the period 1994 to 2007 with the period from 2004 through 2019.

This scaling is based on many assumptions, especially the assumption of a transient steady state. While the large-scale distribution of  $C_{ant}$  has been demonstrated to follow this prediction rather closely, Gruber et al. (2019) pointed out that the reconstructed distribution of the change in  $C_{ant}$  between 1994 and 2007 differs in a few places

considerably from that reconstructed for the period up to 1994. In particular, they found a meridional shift in the accumulation within the Atlantic Ocean, with a reduction in the North Atlantic storage being compensated by an increase in the temperate latitudes of the South Atlantic. Using two different base periods, we attempt to quantify the potential impact of such changes on our conclusions. Direct estimates of the accumulation of  $C_{ant}$  over the same period as analyzed here would be preferable to our scaling approach but are not published to date.

### 3. Uncertainty Assessment

Our method fills very substantial gaps in space and time (see Figure S4 in Supporting Information S1). The GLODAP observations of DIC cover even less of the ocean in horizontal space and time than the surface  $fCO_2$  measurements in the SOCAT database that are used to construct surface ocean flux products (Gregor & Gruber, 2021; Landschützer et al., 2014; Rödenbeck et al., 2015), that is, SOCAT only covers approximately 3% of  $1^\circ \times 1^\circ$  grid cells for any given month across the surface ocean in the 2010s (Gruber et al., 2023). Although GLODAP contains more data points by containing the vertical dimension, that is, interior ocean data, we still have to fill substantial gaps at each depth level. In each year from 2004 through 2019, we have on average  $30 \pm 9$  (mean  $\pm 1$  standard deviation) observations per depth bin. Assuming that this observation was representative of a  $2^\circ \times 2^\circ$  grid at each depth level would mean that only about 0.3% of the global ocean was observed for any given month, requiring that the other 99.7% are filled through our statistical gap-filling methodology. Thus, we emphasize that users keep the different uncertainties in mind when using our product and interpreting our results. Here, we summarize the different sources of uncertainty in our analysis.

#### 3.1. Calculation of the Overall Uncertainty

We identify three main sources of uncertainties that contribute to the total uncertainty of our DIC estimate, following Gregor and Gruber (2021): the uncertainties linked to the measurements ( $M$ ), the representation ( $R$ ), and the prediction ( $P$ ). The overall uncertainty of our DIC estimate ( $DIC_{err}$ ) can then be estimated with standard error propagation:

$$DIC_{err} = \sqrt{M^2 + R^2 + P^2} \quad (3)$$

The uncertainty  $M$  linked to the measurements stems from sampling errors and imprecisions in the measurement system. While GLODAP currently does not report measurement uncertainties, they include a measure of spatial consistency based on inter-cruise comparisons, which amounts to  $2.4 \mu\text{mol kg}^{-1}$  for DIC (Lauvset et al., 2021). We assume that this uncertainty is the same at all grid points, which is likely an overestimation at some points and an underestimation at others.

The representation uncertainty  $R$  results from the fact that the discrete measurements in GLODAPv2.2021 that are used as target data to train the network are taken at one point in time and space and thus might not represent the true monthly mean of the  $1^\circ \times 1^\circ$  grid cell and the depth bin it falls in. Especially problematic are regions where the spatiotemporal variability is high and the number of observations in a grid cell and depth bin is low. It is not straightforward to quantify the representation error as this requires full knowledge of the spatiotemporal variability of DIC. Gregor and Gruber (2021) estimated the representation error of total alkalinity of about  $16 \mu\text{mol kg}^{-1}$  at the sea surface of the open ocean. As the density and spatial distribution of total alkalinity and DIC measurements in GLODAP are similar, and regions with high spatiotemporal variability in total alkalinity tend to be regions of high variability in DIC as well, we adopt this estimate for all grid cells and depth bins. We recognize that alkalinity tends to be less variable than DIC, especially near the surface. In addition, the representation error is expected to be larger near the coast than in the open ocean due to more variability near the coasts and is also expected to decrease with depth (Torres et al., 2021), adding some uncertainty to our uncertainty estimate. Overall, we expect that  $R$  might be underestimated near the surface and the coast and overestimated at depth.

The prediction uncertainty  $P$  represents how well our method can map DIC in time and space. We take the standard deviation across the 15-member ensemble of our bootstrapping approach as our estimate of the prediction error. The differences in the ensemble members are linked to both the ensemble of SOM clusters and the different subsets of training and validation data, as described in Section 2.1. We note that our approach to quantify the prediction uncertainties only considers the spread induced by variations of the method and not the inherent uncertainty of the method itself. Thus, our approach may underestimate the potential errors stemming from the very

**Table 1**

Summary of the Bias, Defined Here as the Mean Difference (MOBO-DIC – Comparison Data Sets), and the RMSD Between MOBO-DIC and the Comparison Data Sets

Compared data set	Type of data	Bias ( $\mu\text{mol kg}^{-1}$ )	RMSD ( $\mu\text{mol kg}^{-1}$ )	MOBO-DIC uncertainty ( $\mu\text{mol kg}^{-1}$ )	Comparison uncertainty ( $\mu\text{mol kg}^{-1}$ )
GLODAPv2.2021	Ship data, without interpolation or mapping (used to train the neural network)	0	16	18	2
Lauvset climatology	Global climatology (optimal interpolation)	7	17	18	7
Broullón climatology	Global monthly climatology (single-step neural network)	10	17	18	N/A
MOBO-DIC <sub>clim</sub>	Global monthly climatology (cluster-regression)	11	20	18	9
HAMOCC	Synthetic data	–1	12	18	N/A
BATS	Time series station	12	17	17	2
HOTS	Time series station	–4	15	17	2
Drake Passage	Time series station (surface)	16	42	18	1
SOCOM floats	Calculated DIC from BGC floats (pH) with LIAR algorithm	–5	14	17	6
OceanSODA-ETHZ	Global surface estimate (cluster-regression)	4	15	18	21

Note. Also displayed are the mean uncertainty of MOBO-DIC at the time and location of the compared data set and the uncertainty of the comparison data sets.

limited time-space distribution of the available data. As this error is difficult to quantify, we rely on our evaluations with independent observations, previous mapped estimates, and synthetic data (Section 4). The global mean prediction uncertainty is  $7 \mu\text{mol kg}^{-1}$ , but with a large spread. We find the highest prediction error in the northern Indian Ocean (up to  $\sim 80 \mu\text{mol kg}^{-1}$ ), where the observations are particularly sparse and where our estimate is heavily extrapolated (Figure S3 in Supporting Information S1). Such large local uncertainties illustrate that our approach can reconstruct global fields, but care must be taken when evaluating regional changes, as the uncertainties on a regional level are quite high. Combining the three uncertainty contributions (Equation 3) yields an overall global mean uncertainty of  $18 \mu\text{mol kg}^{-1}$ .

### 3.2. Quality of Fit

During our mapping approach, we estimate the target data at all grid points. Thus, unlike in an interpolation, there is a difference between the target data (i.e., GLODAPv2.2021) and the mapped estimate (i.e., MOBO-DIC). In Figure S4 in Supporting Information S1, we present these residuals to get a better handle on the quality of our fits. This analysis intends to examine if there are any systematic offsets in different regions or depth levels. It also highlights the magnitude of the differences between the training data and MOBO-DIC. We find that there is no systematic underestimation or overestimation compared to the training data, and the global mean bias cancels out to be 0, while the global mean root mean square difference (RMSD) is  $16 \mu\text{mol kg}^{-1}$  (see Table 1 and Figure S4 in Supporting Information S1), slightly less than our global mean uncertainty of  $18 \mu\text{mol kg}^{-1}$ .

## 4. Evaluation

We evaluate the quality of the mapped MOBO-DIC product with various independent observations and using a synthetic data set derived from a model for which we know the true value. Independence means here that these data were not used for the training of MOBO-DIC (see Table 1 in the Main Text for a summary and Texts S5 and S6, Figures S5–S12 in Supporting Information S1 for a more in-depth analysis of the evaluation).

To evaluate our method with the synthetic data, we subsample the simulated DIC in the biogeochemical component of the Ocean General Circulation Model HAMOCC (Ilyina et al., 2013; Mauritsen et al., 2019) when and where we have observations in GLODAPv2.2021. These synthetic data are pseudo-observations from the HAMOCC model and not real observations. For the oxygen and nutrient fields that we use as predictors, we use the monthly climatologies of these simulated variables to be consistent with our method using real observations. We then run our MOBO-DIC method with these synthetic data to reconstruct the simulated DIC fields. We can then compare our reconstructed fields with the actual DIC in HAMOCC.

For the observations, we use three different sources: First, we use a suite of mapped DIC climatologies, all of which are based on GLODAP data (Broullón et al., 2020; Keppler et al., 2020b; Lauvset et al., 2016). Second, we compare MOBO-DIC with observations from time series stations and biogeochemical Argo floats. Third, we use the mapped surface DIC product contained in OceanSODA-ETHZ (Gregor & Gruber, 2021), allowing us to compare the monthly  $1^\circ \times 1^\circ$  fields at the surface when and where the two data sets overlap (January 2004–December 2018).

We first evaluate the climatological mean, then the trend, and the interannual variability, for each of these evaluation data where the temporal resolution allows. Note that we use DIC and not sDIC in the evaluation with observations, as salinity is not always comeasured, and using monthly  $1^\circ$  gridded salinity fields could introduce errors. In contrast, our comparison of synthetic MOBO-DIC and the HAMOCC model uses sDIC, as here we have both salinity and DIC as monthly  $1^\circ$  gridded fields.

#### 4.1. Evaluation of Climatological Mean

The evaluation of the MOBO-DIC method with the synthetic data from HAMOCC illustrates that the method is well-equipped to reconstruct the mean DIC fields in HAMOCC well (see Table 1). MOBO-DIC reconstructs the simulated climatological mean DIC fields with a negligible bias of  $-1 \mu\text{mol kg}^{-1}$  and with an RMSD of  $12 \mu\text{mol kg}^{-1}$ .

The evaluation with the observational climatological constraints also reveals good performance of MOBO-DIC. The mean differences relative to the Lauvset and Broullón climatologies are between 7 and  $10 \mu\text{mol kg}^{-1}$ , and each has an RMSD of  $17 \mu\text{mol kg}^{-1}$ . This is within the combined uncertainties of MOBO-DIC and the comparison data sets (see Table 1; Figures S5 and S6 in Supporting Information S1). It also needs to be noted that the Lauvset climatology is normalized to the year 2002, while the Broullón monthly climatology is normalized to 1995. Assuming an average surface DIC increase of  $\sim 2 \mu\text{mol kg}^{-1} \text{ yr}^{-1}$ , based on the anthropogenic perturbation, we estimate that the average surface concentration of MOBO-DIC (average year: 2012) is  $\sim 20 \mu\text{mol kg}^{-1}$  higher than the surface Lauvset climatology (normalized to 2002) and  $\sim 34 \mu\text{mol kg}^{-1}$  higher than the surface Broullón monthly climatology (normalized to 1995). The total differences for the Lauvset and Broullón climatologies are less than this as the reported biases in Table 1 are averages over the entire water column, but we observe surface differences on these orders in Supporting Information S1 (Figures S5 and S6).

Surprisingly, the bias and RMSD between the monthly climatology of MOBO-DIC (Keppler et al., 2020a) and this version of MOBO-DIC is larger (11 and  $20 \mu\text{mol kg}^{-1}$ , respectively) than the RMSD between the other two climatologies that are based on different methods, albeit well within the combined uncertainties. The MOBO-DIC climatology is centered around the years 2010/2011, while this study is centered around the year 2012. Thus, the expected surface difference should maximally be of the order of  $\sim 4 \mu\text{mol kg}^{-1}$ . Therefore, we cannot attribute the difference to a change in the periods. Instead, we found that the monthly climatology of MOBO-DIC from Keppler et al. (2020a) contains less DIC in the subsurface equatorial Atlantic and Indian Ocean than the Lauvset climatology (see Figure S4 in Keppler et al. (2020a)), while our new version of MOBO-DIC is more consistent with the Lauvset and Broullón climatologies (see Figure S5 in Supporting Information S1). As there are very little data in the equatorial Atlantic and Indian Ocean, it is difficult to determine which of the estimates lies closer to the true value. We speculate that the true value likely lies closer to the three estimates that are close to each other (Lauvset, Broullón, and this study), than the one that differs (monthly climatology of MOBO-DIC).

The biases between MOBO-DIC and the comparison data sets from time series stations and floats ranges from  $-5$  to  $16 \mu\text{mol kg}^{-1}$ . As the biases are both positive and negative, there is no indication of MOBO-DIC having a systematic bias toward over/underestimating the global carbon content (see Table 1; Figures S9 and S10 in Supporting Information S1). The RMSD between MOBO-DIC and these data range from  $14 \mu\text{mol kg}^{-1}$  for the SOCCOM floats to  $42 \mu\text{mol kg}^{-1}$  for Drake Passage but are mostly between 15 and  $20 \mu\text{mol kg}^{-1}$ , that is, comparable to the mean global uncertainty of MOBO-DIC ( $18 \mu\text{mol kg}^{-1}$ ). In all cases except for Drake Passage, the RMSD is within the combined uncertainties of MOBO-DIC at the location of the compared data set and the uncertainty of the compared data set, using standard error propagation. The disagreement at Drake Passage, a well-observed time series station, is associated with large local variabilities that are not captured in MOBO-DIC and are further discussed in Section 4.3.

Comparing MOBO-DIC at the surface with the surface DIC from OceanSODA-ETHZ, we find that the magnitude and spatial patterns of the mean DIC agree very well, considering they are based on independent data

**Table 2**

*Comparison of the Trends (in  $\mu\text{mol kg}^{-1} \text{decade}^{-1}$ ) and Interannual Variability (IAV, in  $\mu\text{mol kg}^{-1}$ ), Defined as the Standard Deviation in Time (Seasonal Cycle and Trend Removed), From Independent DIC Estimates, and From MOBO-DIC at the Time and Locations of the Independent Data*

	Compared data set → Depth (m) ↓	BATS	MOBO-DIC at BATS	HOT	MOBO-DIC at HOT	Drake Passage (surface)	MOBO-DIC at Drake Passage	SOCCOM floats	MOBO-DIC at SOCCOM floats
Trend	20–40	1	7	5	2	8	1	–20	–9
	100–150	3	8	13	6	N/A	N/A	3	1
	600–800	16	5	4	5	N/A	N/A	19	26
IAV	20–40	5	2	11	4	9	5	4	3
	100–150	4	2	6	2	N/A	N/A	2	2
	600–800	4	1	3	1	N/A	N/A	3	3

*Note.* Due to data sparsity in the observational data, we average the fields over depth slabs (20–40 m, 100–150 m, and 600–800 m). The locations of the stations are illustrated in Supporting Information S1 (Figure S1).

(SOCAT  $\text{pCO}_2$  vs. GLODAP DIC; Bakker et al., 2016; Lauvset et al., 2021). The global mean RMSD between the two data sets is  $15 \mu\text{mol kg}^{-1}$ , and there is a mean bias of approximately  $4 \mu\text{mol kg}^{-1}$ , which is well within the uncertainties (see Table 1; Figures S11a–S11c in Supporting Information S1).

#### 4.2. Evaluation of Trends

Our synthetic MOBO-DIC generally reconstructs both the spatial distribution and magnitude of the trend of sDIC in HAMOCC well, with no indication of a systemic overestimation or underestimation of the trend (see Figure S7 in Supporting Information S1). An exception is the deep eastern equatorial Pacific, where MOBO-DIC overestimates the trend. This could be the result of overfitting or of challenges of MOBO-DIC to fit the trends in a region with very large lateral gradients and where data coverage is intermittent. We do not see similarly large trends in the reconstructions with observations, possibly because the observed lateral gradients are smaller than those in the model. Still, this mismatch in the synthetic data suggests that the MOBO-DIC reconstructed trends are likely somewhat less robust than the climatologies and that care must be taken to avoid an overinterpretation of the results.

The sDIC trends at the time series stations are comparable to MOBO-DIC at the times and locations of these independent observations (see Table 2; Figure S9 in Supporting Information S1). For example, we observe a mean trend in the water column at BATS of  $7 \mu\text{mol kg}^{-1} \text{decade}^{-1}$ , while the mean trend in the water column in MOBO-DIC at the grid cell closest to BATS is  $5 \pm 2 \mu\text{mol kg}^{-1} \text{decade}^{-1}$ . However, some quantitative differences exist, with the largest difference in the trend found at depths between 600 and 800 m at BATS. There, MOBO-DIC, with an estimated trend of only  $5 \pm 2 \mu\text{mol kg}^{-1} \text{decade}^{-1}$  underestimates the observed trend of  $16 \mu\text{mol kg}^{-1} \text{decade}^{-1}$  quite substantially. With BATS being one of the best-constrained time series sites, the observed trend is very robust. The trend is much better reconstructed in the shallower waters at BATS, indicating that this is not a general issue but likely an issue specifically associated with the intermediate water masses in the North Atlantic.

MOBO-DIC also underestimates the trend seen in the BGC-Argo floats in the Southern Ocean (SOCCOM floats) between 20 and 40 m (see Table 2 and Figure S10 in Supporting Information S1). The observed trend is  $-20 \mu\text{mol kg}^{-1} \text{decade}^{-1}$ , while the trend estimate in MOBO-DIC at the same grid cells is only  $-9 \pm 2 \mu\text{mol kg}^{-1} \text{decade}^{-1}$ . There is a known difference between ship-based DIC measurements and DIC derived from float pH measurements (Gray et al., 2018). However, this offset is thought to be relatively steady and should not affect the trend. Nevertheless, the time series is short and spatially sparse, so it is not entirely clear whether the issue is with MOBO-DIC or with the SOCCOM-derived DIC trend.

The trend of MOBO-DIC at the surface has a similar spatial distribution but is slightly smaller than the trend of the mapped surface DIC from Gregor and Gruber (2021), with a global mean trend between January 2004 and December 2018 of  $0.6 \pm 0.1$  and  $0.8 \mu\text{mol kg}^{-1} \text{yr}^{-1}$ , respectively (see Figures S11d–S11f in Supporting Information S1). As OceanSODA-ETHZ is based on considerably more surface measurements than MOBO-DIC, it is likely that MOBO-DIC slightly underestimates the trend of the surface DIC.

### 4.3. Evaluation of Interannual Variability

Similar to the trend, our synthetic MOBO-DIC reconstructs the spatial distribution and magnitude of the interannual variability, defined here as the standard deviation across the ensemble, of sDIC in HAMOCC well (see Figures S8 in Supporting Information S1). However, we also find an artifact in the deep eastern equatorial Pacific, that is, the same region where we had difficulties with the trend. There, the interannual variability is too large in the synthetic MOBO-DIC reconstruction. Again, no such artifact exists in the MOBO-DIC reconstructions with observations, but smaller artifacts cannot be ruled out.

MOBO-DIC tends to underestimate the observed interannual variability of sDIC at the time series stations and the locations of the SOCCOM floats (see Table 2; Figures S9 and S10 in Supporting Information S1). The biggest difference in the interannual variability is between 20 and 40 m at HOT, where MOBO-DIC estimates a variability of only  $4 \mu\text{mol kg}^{-1}$ , while the observations suggest a value of  $11 \mu\text{mol kg}^{-1}$ . As above, such differences can be at least partially explained by the observations containing a lot of noise and not necessarily being representative of the mean monthly  $1^\circ$  fields. At Drake Passage, the comparison data displays considerably more variability than our gridded product and may include outliers. Thus, there are instances where the discrepancies between MOBO-DIC and the comparison data sets are beyond the uncertainty limits. We expect that this is mostly due to large local variabilities that are smoothed out in the monthly mean  $1^\circ \times 1^\circ$  fields in MOBO-DIC.

The interannual variability of MOBO-DIC at the surface also has a similar distribution and is slightly smaller than the interannual variability of the mapped surface DIC from Gregor and Gruber (2021) (see Table 2; Figures S11g–S11i in Supporting Information S1). Here, we observe global mean standard deviations of 3 and  $4 \mu\text{mol kg}^{-1}$ , respectively (see Figures S11g–S11i in Supporting Information S1). An explanation for their slightly higher variability could lie in the fact that OceanSODA-ETHZ uses satellite-based sea surface temperature (SST) as a predictor while we use float data for temperature and salinity. Satellite-based SST estimates are known to display more variability than float-based estimates (Roemmich & Gilson, 2009). Further, OceanSODA-ETHZ has less interannual variability in  $\text{pCO}_2$  than other surface products such as SOM-FFN by Landschützer et al. (2016). Thus, the available evidence suggests that MOBO-DIC tends to underestimate the interannual variability. We suspect that if time-varying monthly fields of oxygen and nutrients were available as predictors, the interannual variability in MOBO-DIC might be larger. In addition, if we had more DIC training data available, the interannual signal could likely be captured better.

## 5. Results and Discussion

### 5.1. Global Changes in the DIC Inventory

The reconstructed (near) global sDIC inventory between 0 and 1,500 m increased steadily from 2004 through 2019, with a total increase of  $42 \pm 5 \text{ Pg C}$  over this period (Figure 1). All depth ranges contribute to this trend, with  $\sim 16\%$  of the increase in sDIC having occurred in the upper 150 m,  $\sim 18\%$  between 150 and 300 m,  $\sim 38\%$  between 300 and 700 m, and  $\sim 28\%$  between 700 and 1,500 m. Superimposed onto this strong positive trend, we observe the effect of the seasonal cycle on the total inventory (order of  $\sim 2 \text{ Pg C}$ ), some interannual variations, and a weakening of the trend in the second half of the record, most strongly visible in the deepest depth slice analyzed, that is, below 700 m.

By adding an estimate of the sDIC changes in the shallow coastal regions and the high latitudes ( $3 \pm 0.4 \text{ Pg C}$ ) and in the ocean below 1,500 m ( $6 \pm 6 \text{ Pg C}$ ; see Text S3 in Supporting Information S1), we arrive at a global sDIC inventory change of  $51 \pm 11 \text{ Pg C}$  over the 16 years of our analysis. This corresponds to an average rate of increase of  $3.2 \pm 0.7 \text{ Pg C yr}^{-1}$ . We interpret this increase in sDIC to be mostly of atmospheric origin, that is, reflecting a net uptake of  $\text{CO}_2$  from the atmosphere, although we cannot exclude a small contribution coming from other sources, such as a trend in the input from rivers and sediment sources, or an imbalance with the marine organic carbon pool.

Our interior ocean data-based net ocean uptake estimate of  $3.2 \pm 0.7 \text{ Pg C yr}^{-1}$  is comparable with surface  $\text{pCO}_2$  observation-based estimates of the net carbon flux from the atmosphere into the ocean. The latest update of the net air-sea  $\text{CO}_2$  flux estimate by Landschützer et al. (2016), which includes both the open and coastal ocean, suggests a global uptake of  $2.1 \pm 0.5 \text{ Pg C yr}^{-1}$  from 2004 through 2019. Adding a riverine outgassing of  $\text{CO}_2$  of  $0.6 \pm 0.4 \text{ Pg C yr}^{-1}$  (Friedlingstein et al., 2022; Regnier et al., 2022), these surface ocean data suggest a net

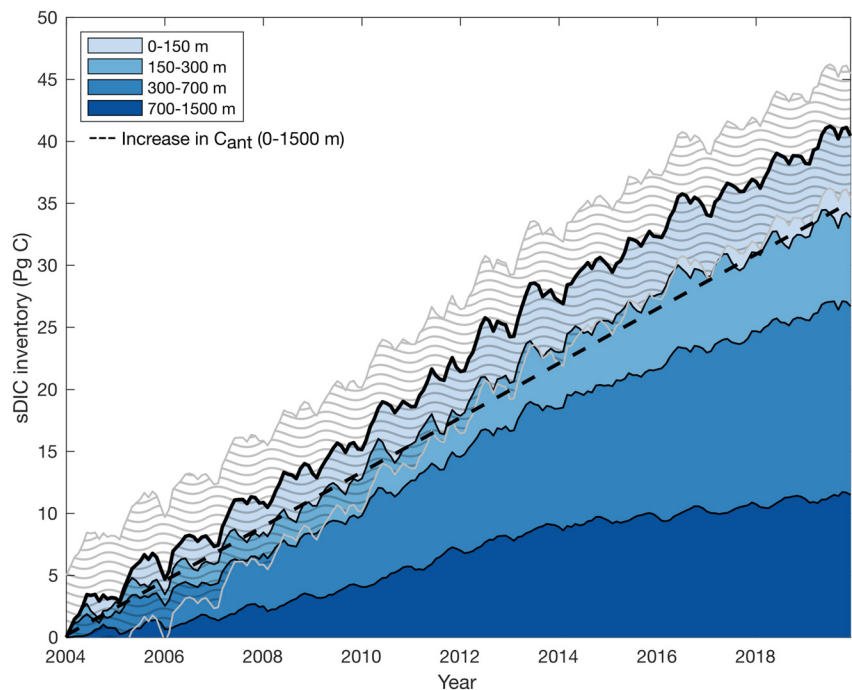


**Figure 1.** Temporal change in the global sDIC inventory derived from MOBO-DIC from 2004 through 2019, relative to January 2004, for different depth slabs: 0–150 m, 150–300 m, 300–700 m, and 700–1,500 m (from light blue to dark blue). The gray shading marks the uncertainty around the upper 1,500 m. The dashed black line illustrates the estimated increase in  $C_{ant}$  based on  $\Delta C_{ant}$  from 1800 to 2007 scaled to the same period, using a scaling factor  $\alpha$  of 0.29.

uptake of  $2.7 \pm 0.6 \text{ Pg C yr}^{-1}$ . Similar numbers are obtained when using an ensemble of surface  $p\text{CO}_2$  data (Fay et al., 2021). This is  $0.5 \pm 0.6 \text{ Pg C yr}^{-1}$  less than our estimate based on the increase in ocean interior sDIC but within the uncertainty bounds. Also, a scaled estimate of the accumulation of anthropogenic  $\text{CO}_2$  in the ocean interior over this time period suggests a global uptake on the order of close to  $3 \text{ Pg C yr}^{-1}$  (Gruber et al., 2023). It has to be noted, as stated above, that there are still uncertainties in the surface-based estimates, due to the indirect approach that needs to incorporate the riverine flux, which has large uncertainties, and a possible skin-temperature correction (Dong et al., 2022; Watson et al., 2020). Specifically, Dong et al. (2022) suggested that the proper accounting of all temperature-related issues (e.g., skin correction) would increase the ocean uptake of the commonly used surface  $p\text{CO}_2$  based products by +35% ( $0.6 \text{ Pg C yr}^{-1}$ ) for the period 1982–2020. If one was to use the skin correction of  $0.6 \text{ Pg C yr}^{-1}$ , as well as the  $0.6 \text{ Pg C yr}^{-1}$  riverine flux, this would yield a total flux of  $3.3 \pm 0.6 \text{ Pg C yr}^{-1}$ , which is remarkably close to our estimate of  $3.2 \pm 0.7 \text{ Pg C yr}^{-1}$ .

Our estimate of the total increase in ocean sDIC of  $51 \pm 11 \text{ Pg C}$  implies that from 2004 through 2019, the ocean sink accounted for  $\sim 31\% \pm 7\%$  of the total anthropogenic  $\text{CO}_2$  emissions (here: from fossil fuel emissions and land use change, Friedlingstein et al., 2022). This uptake fraction is larger but within the uncertainties compared to the fraction reported by the Global Carbon Project based on ocean models and surface ocean  $p\text{CO}_2$  products during the decade 2011–2020 ( $26\% \pm 4\%$ , Friedlingstein et al., 2022). As pointed out by Friedlingstein et al. (2022), within the Global Carbon Budget estimates, it is particularly the hindcast model-based estimates that indicate a smaller uptake. Similarly, Terhaar et al. (2022) used an emergent constraint approach to demonstrate that most CMIP models tend to take up too little  $\text{CO}_2$  from the atmosphere. Although CMIP models differ from the hindcast models used in the Global Carbon Budget, these findings further indicate that the models underestimate the oceanic carbon uptake, as also discussed by Hauck et al. (2020). Our interior ocean-based estimate thus supports the larger (mostly observation-based) estimates of the ocean carbon sink in the Global Carbon Budget, albeit within large uncertainties.

Another reference point is the oceanic accumulation of  $C_{ant}$  between 2004 and 2020. Lacking an estimate of the  $C_{ant}$  accumulation over the same period, we scale the estimates of Sabine et al. (2004) and Gruber et al. (2019) to this period, assuming a transient steady state (see Section 2.4). We obtain a global increase of  $44 \pm 6 \text{ Pg C}$

( $2.8 \pm 0.4$  Pg C yr<sup>-1</sup>) in  $C_{ant}$  (1800–2007 scaled to 2004–2019 with a scaling factor of 0.29) and  $49 \pm 6$  Pg C ( $3.1 \pm 0.4$  Pg C yr<sup>-1</sup>) in  $C_{ant}$  (1994–2007, scaled to 2004–2019 with a scaling factor of 1.45). The estimates are remarkably close to our estimate of the increase in total sDIC ( $51 \pm 11$  Pg C, i.e.,  $3.2 \pm 0.7$  Pg C yr<sup>-1</sup>). This suggests that we can largely attribute the reconstructed increase in the sDIC to the uptake of anthropogenic CO<sub>2</sub> from the atmosphere. Similarly, when only considering the domain of MOBO-DIC and without upscaling, we also find that the trend in MOBO-DIC ( $40 \pm 5$  Pg C, i.e.,  $2.5 \pm 0.3$  Pg C yr<sup>-1</sup>) is close to the increase in  $C_{ant}$  over the same period and domain ( $35 \pm 4$  Pg C, i.e.,  $2.2 \pm 0.2$  Pg C yr<sup>-1</sup>, dashed line in Figure 1) and also well within the uncertainties. Considering the proposed outgassing signal of  $C_{nat}$  (McNeil & Matear, 2013), this would have been reflected in a weaker trend in total sDIC than in  $C_{ant}$ ; however, we do not observe this during our study period. This finding is in-line with the recent review by Gruber et al. (2023) who also concluded that the trend in the oceanic carbon sink was primarily driven by the increasing uptake of  $C_{ant}$  and that the proposed loss of  $C_{nat}$  can at this stage not be conclusively quantified with observations.

Superimposed onto this positive long-term trend of sDIC, the reconstructions reveal substantial interannual variations and a weakening of the trend after ~2012, especially in the deeper waters. The following sections will further discuss these variations and the weakening trend. We also dive deeper into the differences between the anthropogenic component and the total sDIC in the water column, revealing changes in the natural DIC pool. Additionally, we find a strong seasonal signal, most pronounced near the surface. We do not discuss the seasonal variations near the surface, as the seasonal cycle of DIC was explored in Keppeler et al. (2020b).

## 5.2. Regional Distribution of Trends in sDIC, $C_{ant}$ , and $C_{nat}$

The rate of the depth-integrated accumulation of sDIC is regionally strongly structured (Figure 2a), with the highest rates of accumulation found in the North Atlantic south of Iceland, that is, the Subpolar Gyre. There, the linear trend exceeds  $1.5$  mol m<sup>-2</sup> yr<sup>-1</sup>. An additional region with elevated rates of increase can be identified in the Southern Hemisphere between about 20°S and 45°S with typical accumulation rates of ~1 mol m<sup>-2</sup> yr<sup>-1</sup>. The higher latitudes of the Southern Ocean, the tropical regions, the northern Indian, and particularly the North Pacific have considerably weaker depth-integrated changes in sDIC, typically 0.5 mol m<sup>-2</sup> yr<sup>-1</sup> or less. In some regions of the North Pacific, the depth-integrated sDIC even decreases over our study period. This vertical integral is a robust feature of our analysis as it is only weakly changing when removing trends within the water column that are not significant (compare Figure S12 in Supporting Information S1 with Figure 2a).

At each depth level, most of the trends in sDIC are statistically significant (95% confidence interval, see Text S7 and Figure S12 in Supporting Information S1). This is also the case for the negative trends in the North Pacific. Further support comes from the existence of a comparable negative trend in the surface DIC reconstructions of the OceanSODA-ETHZ product (Gregor & Gruber, 2021), as demonstrated in Section 4.2 and Figure S11 in Supporting Information S1. Thus, this negative signal in the North Pacific appears robust within our period and is not an artifact of our method.

Next, we examine the similarity between the rate of depth-integrated accumulation of sDIC and  $C_{ant}$ , which becomes even more evident when they are put side by side, irrespective of how we estimated the expected change in  $C_{ant}$  from 2004 through 2019. The patterns and magnitude of the depth-integrated accumulation of sDIC (Figure 2a) and the two different estimates of  $C_{ant}$  (Figures 2b and 2c) are to the first order approximately the same, as also evidenced by their high pattern correlation coefficient  $c = 0.56$  and  $0.63$ , between the trend in MOBO-DIC and the scaled  $\Delta C_{ant}$  from the combined estimate by Sabine et al. (2004) and Gruber et al. (2019) and the estimate by Gruber et al. (2019), respectively. For example, we observe in all fields a large increase in the North Atlantic and a broad band of enhanced accumulation in the midlatitudes of the Southern Hemisphere. Also present in all fields is the weaker signal in the midlatitude Southern Ocean. This further supports the conclusion that most of the column-integrated change in sDIC can be attributed to the increase in  $C_{ant}$  during this period.

However, there are also several notable differences, discernible when we subtract the estimated anthropogenic component (i.e.,  $\Delta C_{ant}$ ) from the reconstructed change in sDIC (Figures 2d and 2e). This difference can be interpreted as the change in the natural oceanic CO<sub>2</sub> component of DIC, that is,  $\Delta C_{nat}$ , although given our steady-state assumption when estimating  $\Delta C_{ant}$ , this difference can also contain an element of the nonsteady-state, that is, climate variability induced, component of  $\Delta C_{ant}$ . The North Pacific stands out as the region with the biggest loss in  $C_{nat}$ . In addition,  $C_{nat}$  is lost in the upwelling region of the Atlantic sector of the Southern Ocean and

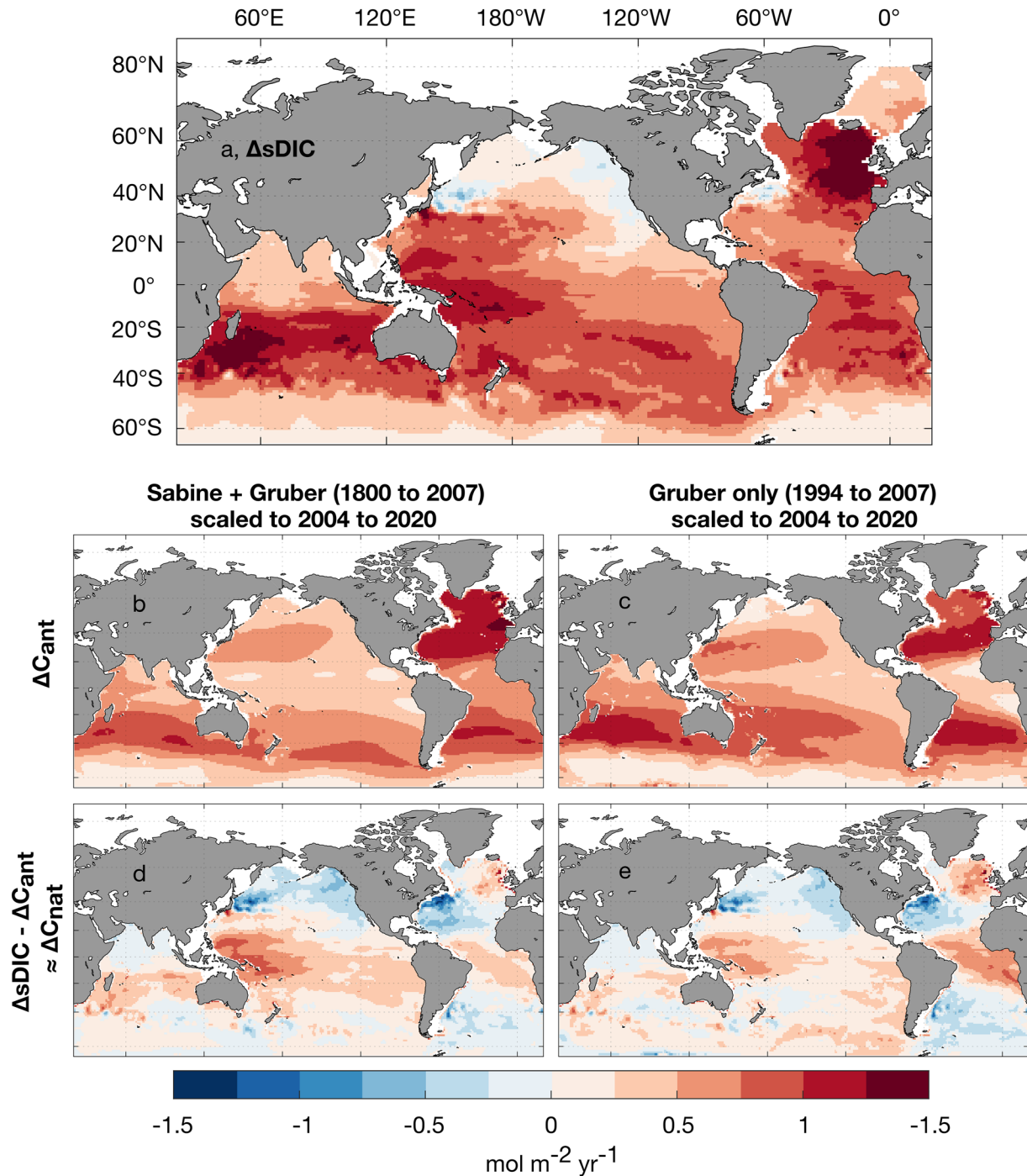


**Figure 2.** Maps of the column-integrated (upper 1,500 m) (a) change in sDIC from 2004 through 2019 based on the linear trend, (b, c) change in  $C_{ant}$  scaled to the same period (2004 through 2019), and (d, e) the anomalous change (i.e., approximately the change in  $C_{nat}$ ) from 2004 through 2019, estimated from the difference between the change in the MOBO-DIC inventory [illustrated in (a)], and the change in the  $C_{ant}$  inventory, scaled to the same period as (a) [illustrated in (b) and (c)]. For the combined estimate of  $C_{ant}$  by Sabine et al. (2004) (1800–1994) and Gruber et al. (2009) (1994–2007) (b, d) and for the estimate of  $C_{ant}$  by Gruber et al. (2009) (1994–2007; c, e). Scaling on the basis of the transient steady-state model ( $anom = \Delta MOBO-DIC - \alpha \cdot \Delta C_{ant}$ ,  $\alpha = 0.29$  for the period 1800–2007 and  $\alpha = 1.45$  for the period 1994–2007). See Figure S12 in Supporting Information S1 for the trends in MOBO-DIC on individual depth levels.

the Subtropical Gyre of the North Atlantic. These losses of  $C_{nat}$  are counter-balanced by gains of  $C_{nat}$  in the tropics and the Indo-Pacific sector of the Southern Ocean. Furthermore, in the North Atlantic Subpolar Gyre, a region of strong uptake of  $C_{ant}$ , we also observe an increase in  $C_{nat}$ . Integrating  $\Delta C_{nat}$  yields a total increase of

$0.4 \pm 0.8$  Pg C yr<sup>-1</sup>, and  $0.1 \pm 0.8$  Pg C yr<sup>-1</sup>, for  $C_{nat}$  based on the combined estimate (Gruber et al., 2019; Sabine et al., 2004) and the estimate by Gruber et al. (2019), respectively. Given the lack of statistical significance, we conclude that we cannot detect a global change in  $C_{nat}$  during our study period.

Nonetheless, the reduction of  $\Delta C_{nat}$  in the North Pacific stands out. We link this change to the phasing of the Pacific Decadal Oscillation (PDO) as it shifted between 2004 and 2019 from positive to negative. While negative PDO regimes are associated with a shallow thermocline in the Kuroshio Extension, which results in deep mixing and cooler SSTs in the North Pacific, positive PDO regimes are associated with warmer SSTs (Mantua & Hare, 2002). Thus, we speculate that during our analysis period, the shoaling of the thermocline in the North Pacific brought DIC stored at depth to the surface, allowing it to outgas, leading to an overall loss of DIC in this region. We expect that the opposite would occur during positive phases of the PDO so that the net change over multiple decades would be close to zero, and thus not impact the long-term trend. To test this hypothesis, we plotted the trend in the surface sDIC from OceanSODA-ETHZ (Gregor & Gruber, 2021) over their entire study period (1985 through 2018). Over that extended period, we do not observe negative trends in surface sDIC in the North Pacific (not shown), indicating that the observed negative trend in the North Pacific sDIC and  $C_{nat}$  between 2004 and 2019 is not a long-term signal. The loss of  $C_{nat}$  in the North Pacific during our analysis period is partially balanced by a gain in  $C_{nat}$  in most parts of the Indo-Pacific, especially in the Western tropical Pacific. We find that this signal is associated with the phasing of the El Niño Southern Oscillation (ENSO), as further discussed in Figure S13 in Supporting Information S1. We speculate that over a longer period than our 16 years, this signal of increased  $C_{nat}$  in the Western tropical Pacific would also be dampened.

Similarly, we link the changes in  $C_{nat}$  in the North Atlantic to the phasing of the Atlantic Multidecadal Oscillation (AMO; Kerr, 2000) as between 2004 and 2019, the AMO index moved from positive to negative (see <https://climatedataguide.ucar.edu/climate-data/atlantic-multi-decadal-oscillation-amo>). Negative AMO phases are associated with increased vertical mixing in the North Atlantic Subpolar Gyre, and thus, an increase of upper ocean DIC and  $C_{nat}$  in this region (Breedon & McKinley, 2016). Concurrently, in the North Atlantic Subtropical Gyre, negative AMO phases are associated with a decrease in DIC and  $C_{nat}$  in this region due to changes in the temperature affecting the solubility of CO<sub>2</sub>. In the tropical Atlantic, the increase in  $C_{nat}$  during our study period might be associated with teleconnections from the AMO phasing. The loss of  $C_{nat}$  in the South Atlantic is in line with the findings by Keppler and Landschützer (2019) who reported a weakening of the Southern Ocean carbon sink in the Atlantic sector since ~2012. They linked this weakening to shifts in sea level pressure and associated changes in surface winds. We note that these links between changes in  $C_{nat}$  and the PDO and the AMO are speculative at this point, as the relatively short temporal extent of MOBO-DIC (16 years) prevents us from robustly concluding on the effect of multidecadal modes of variability.

Figure 3 reveals how the trend in sDIC varies with depth at the scale of entire ocean basins split into latitude bands (black line). Near the surface, sDIC is reconstructed to have increased, on average by about  $0.6 \mu\text{mol kg}^{-1} \text{yr}^{-1}$ , with some regions having a higher accumulation (e.g.,  $0.8 \mu\text{mol kg}^{-1} \text{yr}^{-1}$  in the North Atlantic) and other regions less (e.g.,  $0.3 \mu\text{mol kg}^{-1} \text{yr}^{-1}$  in the North Pacific). In all regions, the trend in sDIC increases between the mixed layer and the intermediate waters and then decreases with depth below that, reaching values of around  $0.2 \mu\text{mol kg}^{-1} \text{yr}^{-1}$  at 1,500 m. We observe the largest increase in sDIC in the Atlantic between ~200 and 500 m ( $\sim 0.9 \mu\text{mol kg}^{-1} \text{yr}^{-1}$ ).

Comparing the temporal trends in sDIC with the estimated changes in  $C_{ant}$  (blue and red lines in Figure 3) highlights strong similarities but also distinct differences. Near the surface, sDIC increased less than  $C_{ant}$  during our study period. This difference is significant in all regions except for the Southern Ocean and North Atlantic. In the deeper ocean, the difference between the trend in sDIC and  $\Delta C_{ant}$  is not significant in the Southern Ocean, North Pacific, tropical Indian Ocean, and the South Atlantic, while in the other regions, the trend in sDIC tends to be larger than the two estimates of  $\Delta C_{ant}$ . The differences between the trends in sDIC compared to those in  $C_{ant}$  imply a loss of  $C_{nat}$  in the upper ocean and a gain of  $C_{nat}$  in the ocean's interior below a few hundred meters depth. Combined with the lack of an overall change in  $C_{ant}$ , this suggests a strong internal redistribution of oceanic  $C_{nat}$  over our analysis period.

We tested the robustness of our inferred ocean internal redistribution of  $C_{nat}$  by comparing them to data from repeat hydrographic lines obtained as part of the Global Ocean Ship-based Hydrographic Program (GO-SHIP; Talley et al., 2016). In Figure S14 in Supporting Information S1, we compare the change in DIC between different occupations of the same line with the reconstructed change in MOBO-DIC at the same locations over the same

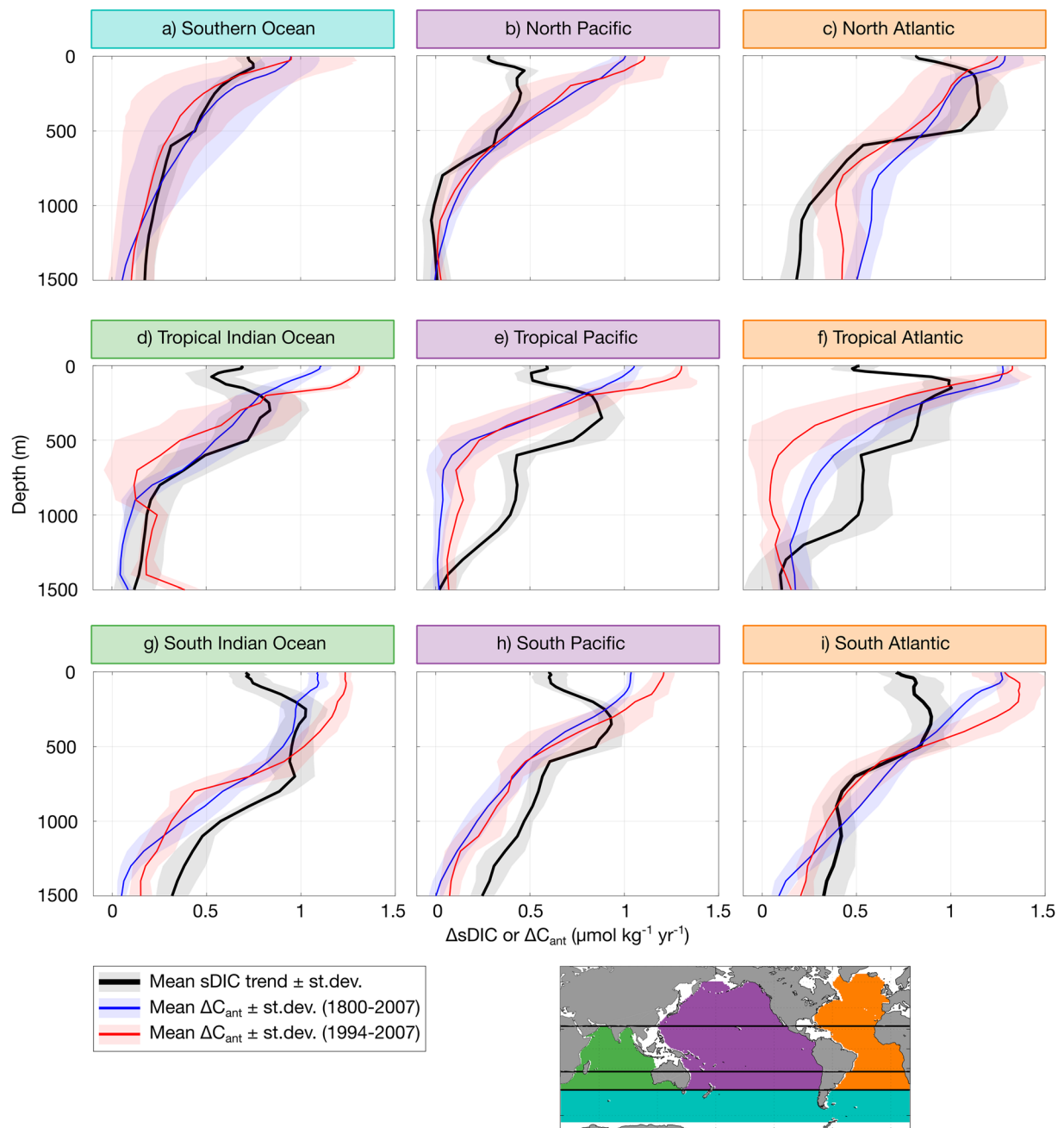


**Figure 3.** Vertical profiles of the mean trend in subregions for sDIC estimated by MOBO-DIC (black) and  $\Delta C_{ant}$  from 1800 to 2007 scaled to the period 2004 through 2019 (blue) and from 1994 to 2007, scaled to 2004 through 2019 (red). The uncertainty of the trend in sDIC, based on the standard deviation across the trend in the 15 ensemble members, is illustrated in shading. The uncertainty of the trend in  $\Delta C_{ant}$ , based on the standard deviation in the latitude-longitude space, is illustrated in shading. Separately for the Southern Ocean (a), Indian Ocean (d, g), Pacific (b, e, h), Atlantic (c, f, i), in the northern temperate regions (until 23°N, b, c), the tropics (23°N–23°S, d–f), and in the southern temperate regions (from 23°S to 40°S, g–i). The map at the bottom indicates the limits of the ocean basins in color, and the climatic regions are delimited by black lines.

period, and also with the changes in  $C_{ant}$  scaled to the same period. We find that the change in DIC (both at the repeated GO-SHIP tracks and in MOBO-DIC) differs substantially from the  $\Delta C_{ant}$  profiles, in a similar way as demonstrated when we average over large regions in Figure 3. This adds a second line of evidence that the vertical redistributions of  $C_{nat}$  that we discuss here are not artifacts from our method but are also directly visible in the ship measurements from the GO-SHIP program. We note that the magnitude of the trend in DIC is larger when only considering the grid cells of the GO-SHIP tracks (Figure S14 in Supporting Information S1) than when

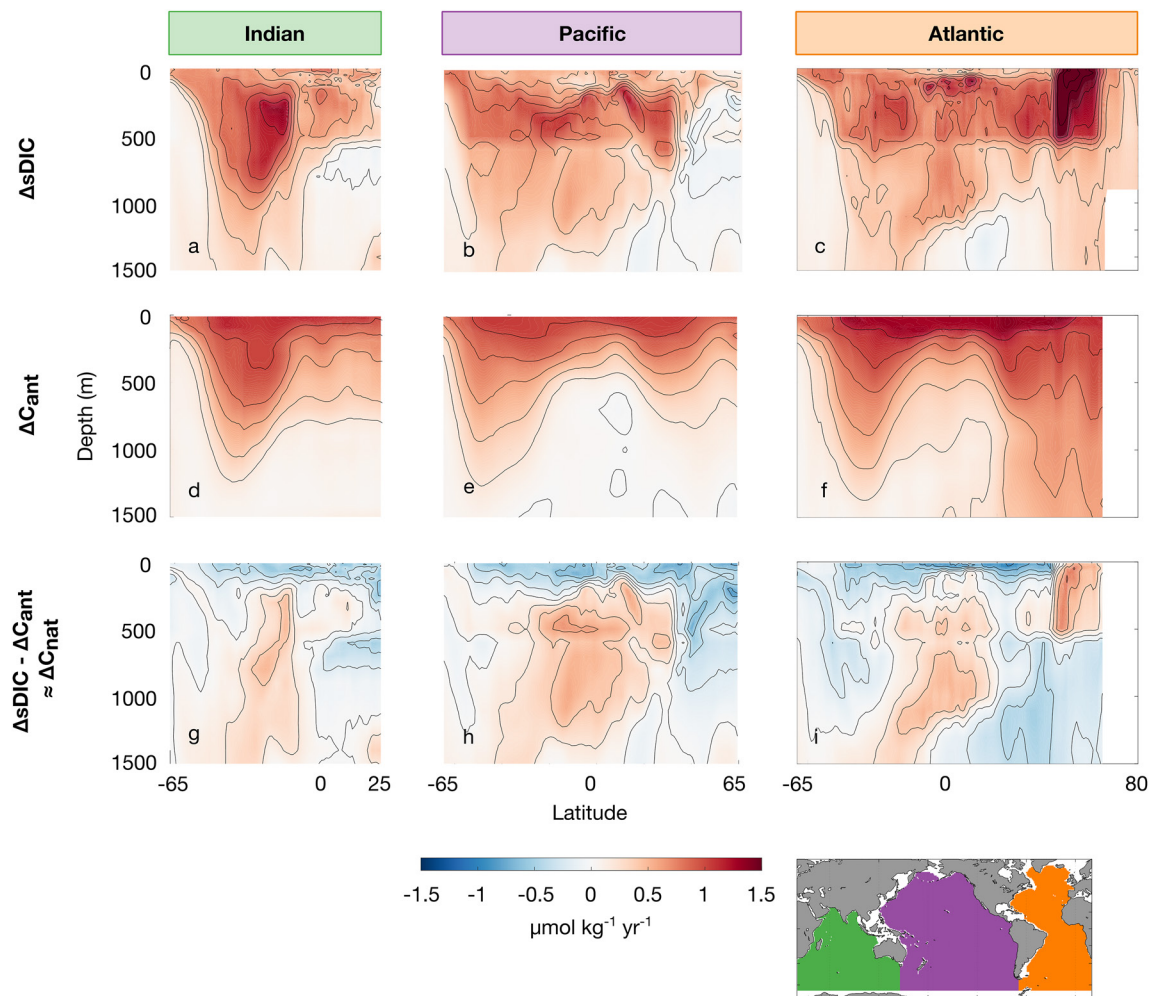


**Figure 4.** Zonal mean sections of the trend in sDIC from 2004 through 2019 (a–c), of  $\Delta C_{ant}$  from 1800 to 2007, scaled to our period (d–f), and the difference between the two, that is,  $\Delta C_{nat}$  (g–i), for the Indian Ocean (a, d, g), Pacific (b, e, h), and the Atlantic (c, f, i). The map at the bottom right illustrates the boundaries of the basins.

averaging over large regions (Figure 3) due to a tendency for opposing trends canceling each other when the profiles are averaged over large regions.

The similarities and differences in the vertical distribution of the trends in sDIC,  $C_{ant}$ , and  $C_{nat}$  become even more evident when analyzing zonal mean sections of these components (Figure 4). Due to methodological constraints, there are some discontinuities at 500 m in the MOBO-DIC derived sDIC (Figures 4a–4c), which are associated with boundaries generated by the depth slabs. Aside from that, the trend in sDIC and  $\Delta C_{ant}$  (Figures 4d–4f) are very similar, as noted above for the mean profiles. This figure again highlights the loss of  $C_{nat}$  (Figures 4g–4i) at the surface, except in the North Atlantic. We also observe a loss of  $C_{nat}$  in the North Pacific, extending down to 1,500 m but most pronounced in the upper ~800 m. The northern high latitudes tend to lose  $C_{nat}$  at depth, while the low latitudes tend to gain  $C_{nat}$  at depth. Overall, the redistribution of  $C_{nat}$  occurs both horizontally, as demonstrated in Figure 2, and vertically (Figures 3 and 4), but as pointed out above, the signal in  $C_{nat}$  is within the uncertainty bounds.

We cannot identify the potential reasons for this redistribution, but the upper ocean loss of  $C_{nat}$  may be at least partially driven by the warming of the ocean, which is strongest in the upper ocean (IPCC, 2021). In addition, such a redistribution pattern is reminiscent of the impact of the ocean's biological pump, where an increased efficiency of this pump would lead to a depletion of  $C_{nat}$  in the upper ocean and an accumulation at depth. As we observe this pattern most prominently in the tropics, we speculate that biology may be driving the change in sDIC here. Conversely, as we already hypothesized above, the other regions, including the North Pacific, North Atlantic, and Southern Ocean are likely driven by physical changes.

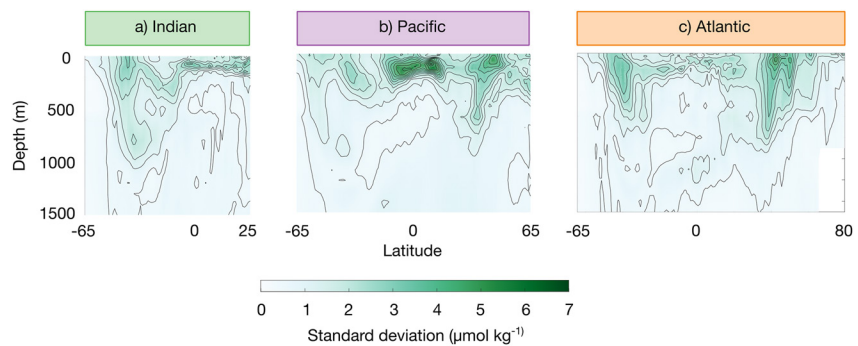


**Figure 5.** Zonal mean sections of the interannual variability of sDIC, defined as the standard deviation of the time-dimension of sDIC (detrended, seasonal cycle smoothed with a 12-month running mean) for the Indian (a), Pacific (b), and Atlantic Oceans (c). See the map at the bottom right of Figure 4 for the boundaries of the basins.

It should also be noted that the vertical profile in the trend is strongly influenced by interannual variations, such as variations in the thermocline and surface outgassing. Thus, the signal in the mixed layer is prone to large interannual to decadal variations, which are especially dominant in the Southern Ocean (Keppler & Landschützer, 2019; Landschützer et al., 2015; Le Quéré et al., 2007). Therefore, the observed trends in the mixed layer depend greatly on the start and end year and should be interpreted with care. A longer time series would yield a result more representative of the anthropogenically forced trend.

### 5.3. Interannual Variability at Global and Basin-Scale

The interannual variability of sDIC, defined here as the standard deviation in time (seasonal cycle and trend removed), is rather small in our product, especially when compared to the magnitude of the trend (previous section) and the amplitude of the seasonal cycle (Keppler et al., 2020b). With a global mean temporal standard deviation of  $2 \mu\text{mol kg}^{-1}$  at 150 m (the depth level with the largest mean standard deviation), compared to a global mean uncertainty of  $18 \mu\text{mol kg}^{-1}$  at 150 m, the interannual variability is well within the product uncertainty of MOBO-DIC in most parts of the ocean. However, as highlighted in Section 4.3, MOBO-DIC likely underestimates the interannual variability.

Nevertheless, some clear regional signals of the interannual variability emerge (Figure 5): the largest interannual signal is generally in the thermocline region ( $\sim 150$  m), while in the mixed layer and below 700 m, the interannual variability is minimal. The equatorial Pacific stands out as a region with the largest variance, while we observe very little interannual variability in the Southern Ocean, a region with large decadal variability in the air-sea  $\text{CO}_2$  flux estimates (Keppler & Landschützer, 2019; Landschützer et al., 2015; Le Quéré et al., 2007). A recent study has suggested that the decadal variations of the air-sea  $\text{CO}_2$  fluxes in the Southern Ocean may be overestimated in the mapped surface estimates (Gloege et al., 2021); however, the strongest variations occur around the year 2000 (see, e.g., Friedlingstein et al., 2022), that is, before the start of our time series here.

We further illustrate the nature of the mean vacillations of the vertically integrated sDIC (upper 1,500 m) for large subregions in Figure 6. The most dominant interannual variations are found in the Pacific, where we see a steep increase in sDIC between 2010 and 2014 in the tropics. The northern temperate Pacific also stands out. Here, the trend in sDIC is initially weak until 2010, increases until 2014, and then we observe a negative trend until the end of the time series in December 2019. Both in the northern and southern temperate regions of the Atlantic, the sDIC trend has weakened since around 2012. In contrast, averaged over the whole Southern Ocean, we find very few interannual variations here. Similarly, the Indian Ocean, the South Pacific, and the tropical Atlantic all vary little interannually in the upper 1,500 m when averaging over these areas.

We link the sDIC increase in the tropical Pacific at least partially to a shift from La Niñas (especially in 2008 and 2011) to El Niños (especially in 2015 and 2019, see Figure S13 in Supporting Information S1). The other ENSO-related signals during our study period are considerably weaker and seem mostly dampened when considering the whole tropical Pacific. The large variation in the North Pacific is likely to be influenced by the phasing of the PDO, but may also have an ENSO-related teleconnection. We find that the weakening of the vertically

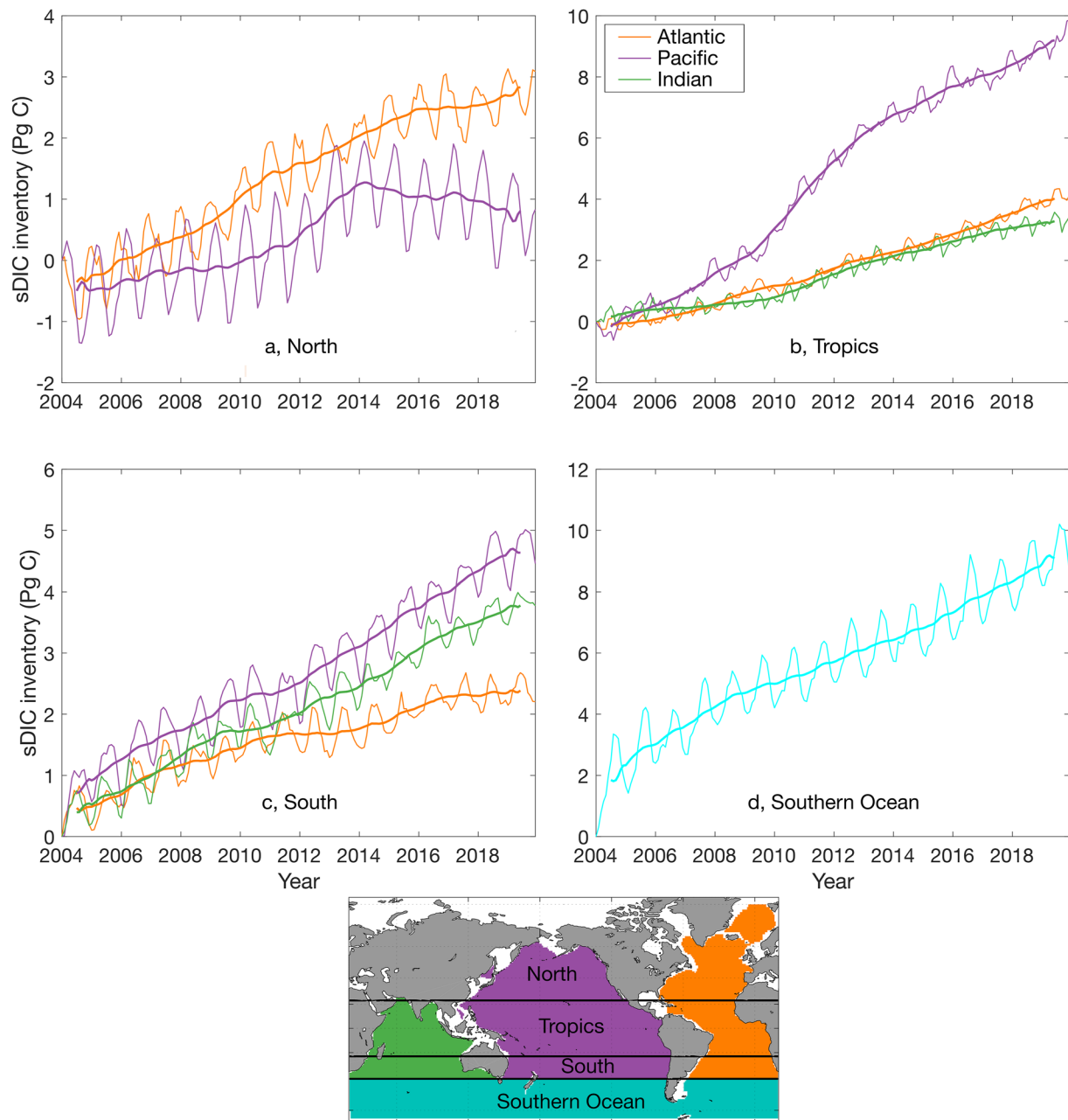


**Figure 6.** Timeline of the vertical integral (upper 1,500 m) of sDIC relative to January 2004 (thin solid lines) in the northern temperate regions (a), tropics (b), southern temperate regions (c), and the Southern Ocean. In (a–c), separately for the Atlantic (orange), Pacific (purple), and Indian Ocean (green). Note that the y-axes differ in each subplot. Thick solid lines have the seasonal cycle smoothed with a 12-month moving average (first and last 6 months removed). The inserted map illustrates the boundaries of the subregions.

integrated sDIC around 2012, illustrated in Figure 1, stems largely from the high latitude South Atlantic and the tropical Pacific. The weakening of the sink in the high latitude South Atlantic is in line with the findings by Keppler and Landschützer (2019), who report a weakening of the CO<sub>2</sub> uptake in the Atlantic sector of the Southern Ocean around 2012. While this signal is not dominant when averaging over the whole Southern Ocean, this weakening sink around 2012 is also visible in the global changes in sDIC (Figure 1), highlighting the important role of the Southern Ocean carbon uptake (here: specifically its Atlantic sector) globally. A longer time series is needed to investigate if this is a long-term decline or part of multidecadal oscillations, such as the AMO. We know from previous studies that this weakening may be due to changes in the circulation, as suggested by DeVries et al. (2017) or linked to atmospheric circulation, as proposed by Keppler and Landschützer (2019).

An alternative hypothesis for these changes is that volcanoes are the driving force for such sudden changes (McKinley et al., 2020). However, during our study period, no large volcanic eruptions occurred that may explain the observed signals.

## 6. Caveats and Uncertainties

Given the sparsity of DIC observations, our product fills substantial observational gaps in time and space. However, our evaluation with independent data provides confidence in the robustness of the presented numbers within the uncertainty limits. Nonetheless, there are good reasons to conclude that MOBO-DIC tends to underestimate the trend and interannual variability. Although this underestimation is within the uncertainty limits, it could be significant when integrating in the water column (see Main Text Section 4 and Texts S5 and S6 in Supporting Information S1). Further research should be conducted on this, especially as more data becomes available with future GLODAP releases and BGC Argo data.

The uncertainties of the MOBO-DIC estimated sDIC at the level of a single grid cell are relatively large (global mean of  $18 \mu\text{mol kg}^{-1}$ ) and are often larger than the signal in the trend or variability. As our mapping method minimizes the overall bias between the target data (i.e., the GLODAP DIC measurements) and the mapped estimate, we can assume that any local imprecisions average out when integrating or averaging over large areas. This means that MOBO-DIC is most robust when considering large areas, while analyses at single grid cells should be interpreted carefully, keeping in mind the uncertainty bounds. In this study, we present such integrals and averages over whole ocean basins.

We want to note that the linear trend analysis used to quantify and assess the long-term changes in DIC has its limitations, too. First, it is not a given that the increase in oceanic carbon is, in fact, linear. Second, the linear trends are based on a relatively short period of 16 years, and thus, the conditions of the start and end years tend to considerably affect the trend over such a short period (Fay & McKinley, 2013). Furthermore, decadal variations might also affect the linear trends. We found that, locally, some trends are not robust (see Figure S12 in Supporting Information S1) but anticipate that our global trend estimate is robust within the uncertainty, as overestimates of the trend in some regions are likely to be balanced by underestimates elsewhere.

Our comparison with  $C_{ant}$  also relies on many assumptions. First, as there is not yet a published estimate of  $C_{ant}$  for the current period, we scaled previous estimates to our period, assuming a steady state (see Section 2.4). Further, our estimate of  $C_{nat}$  is based on the difference in the change in total sDIC and  $\Delta C_{ant}$ . However, due to the steady-state assumption when estimating  $\Delta C_{ant}$ , the difference may also contain an element of the nonsteady-state component of anthropogenic  $\Delta C_{ant}$ . Thus, the analyses with  $C_{ant}$  and  $C_{nat}$  could be improved in the future by using a  $C_{ant}$  estimate of the same period.

## 7. Summary and Conclusions

This release of the Mapped Observation-Based Oceanic Dissolved Inorganic Carbon (MOBO-DIC) extends the climatological estimate by Keppler et al. (2020b) in time, thus giving insights into the spatiotemporal evolution of the ocean DIC stock at a monthly resolution from January 2004 through December 2019. With a spatial resolution of  $1^\circ$ , extending from  $65^\circ\text{N}$  to  $65^\circ\text{S}$  and until  $80^\circ\text{N}$  in the Atlantic and covering the entire upper and middle ocean (depths from 2.5 to 1,500 m on 28 uneven depth levels) this data set provides a near-global view. We conducted an in-depth validation of our new data product, which considers sources of uncertainties from the measurements, representation errors, and uncertainties stemming from our mapping method. We trust that our estimate of DIC is robust within the uncertainty ranges provided (global mean uncertainty at the individual grid cell level of  $18 \mu\text{mol kg}^{-1}$ ).

Our analysis of the trend in sDIC provides the first direct assessment of the changes in the total sDIC stock (natural + anthropogenic) based on observations. It should be noted that at large scales, the changes in sDIC and DIC are numerically equal because the trend in salinity is negligible once integrated vertically and over large regions (Cheng et al., 2020). Our estimate of the global increase of sDIC during our study period ( $3.2 \pm 0.7 \text{ Pg C yr}^{-1}$ ) is approximately  $31\% \pm 7\%$  of the anthropogenic  $\text{CO}_2$  emissions from fossil fuels and land use change during our study period (Friedlingstein et al., 2022). We find that this increase in sDIC is largely associated with the increase in anthropogenic carbon ( $C_{ant}$ ) during this period ( $2.8 \pm 0.4 \text{ Pg C yr}^{-1}$  or  $3.1 \pm 0.4 \text{ Pg C yr}^{-1}$ , depending on the method).

MOBO-DIC also allows for the first assessment of changes in natural oceanic carbon ( $\Delta C_{nat}$ ) by subtracting  $\Delta C_{ant}$  from the changes in the total sDIC, yielding a statistically insignificant global mean  $\Delta C_{nat}$  of  $0.4 \pm 0.8 \text{ Pg C yr}^{-1}$  or  $0.1 \pm 0.8 \text{ Pg C yr}^{-1}$ , depending on the method used to estimate  $C_{ant}$ . Previous studies had suggested a potential outgassing of  $C_{nat}$  due to elevated sea surface temperatures (McNeil & Matear, 2013), which would affect the global climate. While the large uncertainties in MOBO-DIC and  $C_{ant}$  do not rule out such a net outgassing signal of  $C_{nat}$ , we observe no statistically detectable change in  $C_{nat}$  between 2004 and 2020, in-line with the recent review by Gruber et al. (2023). Instead, our analysis reveals a redistribution of  $C_{nat}$ —a phenomenon that had not been previously investigated at a global scale. During our study period, the upper ocean appears to have mostly lost  $C_{nat}$ , while below that, large parts of the ocean increased in  $C_{nat}$ . The loss of  $C_{nat}$  near the surface could be driven by increased ocean temperatures, as proposed by IPCC (2021). The redistributions in the Pacific correspond to the phasing of ENSO and the PDO, while the redistributions in the North Atlantic correspond to the phasing of the Multidecadal AMO. However, at this stage, our study period from 2004 through 2019 is too short to robustly conclude on (multi)decadal signals.

The interannual variability in sDIC is substantially weaker than the seasonal cycle and temporal trend in most parts of the ocean. However, it should be noted that MOBO-DIC likely underestimates the interannual variability. We find a mean standard deviation in time of detrended, deseasonalized sDIC at the depth level with the largest variability (150 m) of  $2 \mu\text{mol kg}^{-1}$ . Our results demonstrate that most of the global-scale variations in sDIC stem from the North and tropical Pacific, in correspondence with ENSO and the PDO, and to a lesser extent from the high latitude South Atlantic. We further find a weakening of the positive trend in the high-latitude South Atlantic around the year 2012. This signal is also visible in the global integral of sDIC, and future studies should examine the continued evolution of this signal as well as its drivers. The interannual variations are comparably weak in the other sectors of the Southern Ocean and the Indian Ocean.

We can now constrain the ocean carbon sink from surface measurements in combination with riverine flux estimates (previous studies) and based on the direct DIC measurements that reflect the changes in the DIC pool at timescales from subannual to interannual (this study). While the surface-based estimates benefit from more observations, large uncertainties are associated with such an indirect approach. The interior perspective suffers from considerably less data but, due to the direct approach, does not need a riverine flux adjustment or gas transfer parametrization. The two perspectives each have their strengths and weaknesses, so having both perspectives substantially improves our understanding and the quantification of the global ocean carbon sink. The two estimates are in good agreement ( $3.2 \pm 0.7 \text{ Pg C yr}^{-1}$  and  $2.7 \pm 0.6 \text{ Pg C yr}^{-1}$  for the interior and surface perspective, respectively), despite being based on independent data (SOCAT vs. GLODAP). However, the surface-based estimates would be larger (i.e., closer to our estimate) when considering a larger riverine flux estimate (e.g.,  $0.8 \pm 0.4 \text{ Pg C yr}^{-1}$  by Resplandy et al. (2018), compared to  $0.6 \pm 0.4 \text{ Pg C yr}^{-1}$  by Friedlingstein et al. (2022) used in this study). In addition, the agreement between the surface-based estimates and our interior ocean estimate would be even higher if the proposed temperature corrections were applied to the surface estimates. Specifically, Dong et al. (2022) estimated that accounting for these corrections would increase the ocean uptake of the surface  $\text{pCO}_2$  based products by  $0.6 \text{ Pg C yr}^{-1}$  from 1982 through 2020.

Further, within the Global Carbon Budget (Friedlingstein et al., 2022), the observation-based methods that estimate the carbon fluxes based on surface measurements are higher than the model-based estimates. Our analysis from the interior ocean perspective suggests that the true value likely lies closer to the observation-based surface estimates in the Global Carbon Budget than to the model-based estimates, as also suggested by Terhaar et al. (2022). Thus, the current approach of averaging all ocean carbon sink estimates from observations and models in the Global Carbon Budget could be revisited and improved to obtain the best estimate, for example, by weighting the observation-based estimates stronger than the models.

Our new data product is available for the scientific community and can be used to further investigate the temporal changes in DIC and its effect on marine organisms. Potential further insights into the processes and drivers could be gained by prolonging the timespan and investigating the multidecadal variations. Additionally, our product provides the basis to compare the decadal variations of observation-based DIC to the changes in the upper Meridional Overturning Circulation, which weakened in the 1980s, strengthened in the 1990s, and weakened again in the 2000s (DeVries et al., 2017). Similarly, further comparing the decadal variations of the Southern Ocean carbon sink (Keppler & Landschützer, 2019; Landschützer et al., 2015; Le Quéré et al., 2007) to the variations in the DIC pool in this region could lead to important new insights on the global carbon cycle.

## Data Availability Statement

The MOBO-DIC data product created during this study is freely available from NCEI/OCADS: <https://www.ncei.noaa.gov/data/oceans/ncei/ocads/metadata/0277099.html> and should be cited as Keppler, Lydia; Landschützer, Peter; Lauvset, Siv K.; Gruber, Nicolas (2023). Mapped Observation-Based Oceanic Dissolved Inorganic Carbon Monthly fields from 2004 through 2019 (MOBO-DIC2004-2019) (NCEI Accession 0277099). [indicate subset used]. NOAA National Centers for Environmental Information. Dataset. <https://doi.org/10.25921/z31n-3m26>. Accessed [date].

The GLODAP DIC ship measurements are available at <https://www.ncei.noaa.gov/data/oceans/ncei/ocads/data/0237935/>. The mapped Argo-based fields of temperature and salinity are available at [https://sio-argo.ucsd.edu/RG\\_Climatology.html](https://sio-argo.ucsd.edu/RG_Climatology.html). The WOA-mapped climatologies of silicic acid, nitrate, and dissolved oxygen are available at <https://www.nodc.noaa.gov/OC5/woa18/woa18data.html>. The atmospheric pCO<sub>2</sub> based on the GlobalView xCO<sub>2</sub> is available at [https://www.nodc.noaa.gov/ocads/oceans/SPCO2\\_1982\\_present\\_ETH\\_SOM\\_FFN.html](https://www.nodc.noaa.gov/ocads/oceans/SPCO2_1982_present_ETH_SOM_FFN.html). The mapped annual climatology of DIC is available at <https://www.ncei.noaa.gov/data/oceans/ncei/ocads/data/0162565/mapped/>. The time series data from HOT, BATS, and Drake Passage are available at <http://hahana.soest.hawaii.edu/hot/hot-dogs/bextraction.html>, <http://bats.bios.edu/bats-data/>, and <https://www.nodc.noaa.gov/archive/arc0118/0171470/2.2/data/0-data/>, respectively. The DIC estimated based on BGC-Argo floats in the Southern Ocean (SOCCOM floats) is available at <http://socompu.princeton.edu/www/index.html>. The OceanSODA surface DIC fields are available at <https://www.ncei.noaa.gov/access/metadata/landing-page/bin/iso?id=gov.noaa.nodc:0220059>. The MOBO-DIC monthly climatology is available at <https://www.ncei.noaa.gov/access/metadata/landing-page/bin/iso?id=gov.noaa.nodc%3A0221526>. The monthly climatology of DIC by Broullón et al. (2020) is available at <https://doi.org/10.20350/digitalCSIC/10551>. The data for C<sub>ant</sub> are available at [https://www.ncei.noaa.gov/access/ocean-carbon-data-system/oceans/ndp\\_100/ndp100.html](https://www.ncei.noaa.gov/access/ocean-carbon-data-system/oceans/ndp_100/ndp100.html) and <https://www.ncei.noaa.gov/access/metadata/landing-page/bin/iso?id=gov.noaa.nodc:0001644> for the periods 1800 to 1994 and 1994 to 2007, respectively. We use the bathymetry from Etopo2 (2001), and the Multivariate El Niño Index (MEI; Wolter and Timlin (2011); <https://psl.noaa.gov/enso/mei/>).

## Acknowledgments

The research leading to these results has received funding from the European Community's Horizon 2020 Project under grant agreement no. 821003 (4C). This work was also sponsored by NSF's Southern Ocean Carbon and Climate Observations and Modeling (SOCCOM) Project under the NSF Awards PLR-1425989 and OPP-1936222, with additional support from NOAA and NASA. The authors are grateful for the Argo data collected and made freely available by the International Argo Program and the national programs that contribute to it (<https://www.argo.ucsd.edu> and <https://argo.jcommops.org>). The Argo Program is part of the Global Ocean Observing System. This publication uses Hawaii Ocean Time series observations supported by the U.S. National Science Foundation under Grant OCE-1260164. It also used data from the Southern Ocean Carbon and Climate Observations and Modeling project (SOCCOM). Data were collected and made freely available by SOCCOM, funded by the National Science Foundation, Division of Polar Programs (NSF PLR-1425989), supplemented by NASA and by the International Argo Program and the NOAA programs that contribute to it. This work benefited from discussions with Birgit Klein (BSH), Jochem Marotzke (MPI-M), Johanna Baehr (UHH), and Jens D. Müller (ETHZ).

## References

- Bakker, D. C. E., Pfeil, B., Landa, C. S., Metzl, N., O'Brien, K. M., Olsen, A., et al. (2016). A multi-decade record of high-quality fCO<sub>2</sub> data in version 3 of the Surface Ocean CO<sub>2</sub> Atlas (SOCAT). *Earth System Science Data*, 8(2), 383–413. <https://doi.org/10.5194/essd-8-383-2016>
- Bates, N. R., Astor, Y. M., Church, M. J., Currie, K., Dore, J. E., Gonzalez-Davila, M., et al. (2014). A time-series view of changing surface ocean chemistry due to ocean uptake of anthropogenic CO<sub>2</sub> and ocean acidification. *Oceanography*, 27(1), 126–141. <https://doi.org/10.5670/oceanog.2014.16>
- Bittig, H. C., Maurer, T. L., Plant, J. N., Schmechtig, C., Wong, A. P. S., Claustre, H., et al. (2019). A BGC-Argo guide: Planning, deployment, data handling and usage. *Frontiers in Marine Science*, 6. <https://doi.org/10.3389/fmars.2019.00502>
- Bittig, H. C., Steinhoff, T., Claustre, H., Fiedler, B., Williams, N. L., Sauzède, R., et al. (2018). An alternative to static climatologies: Robust estimation of open ocean CO<sub>2</sub> variables and nutrient concentrations from T, S, and O<sub>2</sub> data using Bayesian neural networks. *Frontiers in Marine Science*, 5. <https://doi.org/10.3389/fmars.2018.00328>
- Boyer, T. P., Garcia, H., Locarnini, R., Zweng, M., Mishonov, A. V., Reagan, J., et al. (2018). World Ocean Atlas 2018 [Dataset]. NOAA National Centers for Environmental Information. Retrieved from <https://www.ncei.noaa.gov/archive/accession/NCEI-WOA18>
- Breeden, M. L., & McKinley, G. A. (2016). Climate impacts on multidecadal pCO<sub>2</sub> variability in the North Atlantic: 1948–2009. *Biogeosciences*, 13(11), 3387–3396. <https://doi.org/10.5194/bg-13-3387-2016>
- Brewer, P. G. (1978). Direct observation of the oceanic CO<sub>2</sub> increase. *Geophysical Research Letters*, 5(12), 997–1000. <https://doi.org/10.1029/GL005i012p00997>
- Broullón, D., Pérez, F. F., Velo, A., Hoppema, M., Olsen, A., Takahashi, T., et al. (2019). A global monthly climatology of total alkalinity: A neural network approach. *Earth System Science Data*, 11(3), 1109–1127. <https://doi.org/10.5194/essd-11-1109-2019>
- Broullón, D., Pérez, F. F., Velo, A., Hoppema, M., Olsen, A., Takahashi, T., et al. (2020). A global monthly climatology of oceanic total dissolved inorganic carbon: A neural network approach. *Earth System Science Data*, 12(3), 1725–1743. <https://doi.org/10.5194/essd-12-1725-2020>
- Carter, B. R., Feely, R. A., Wanninkhof, R., Kouketsu, S., Sonnerup, R. E., Pardo, P. C., et al. (2019). Pacific anthropogenic carbon between 1991 and 2017. *Global Biogeochemical Cycles*, 33(5), 597–617. <https://doi.org/10.1029/2018GB006154>
- Carter, B. R., Feely, R. A., Williams, N. L., Dickson, A. G., Fong, M. B., & Takeshita, Y. (2018). Updated methods for global locally interpolated estimation of alkalinity, pH, and nitrate. *Limnology and Oceanography: Methods*, 16(2), 119–131. <https://doi.org/10.1002/lom3.10232>
- Chen, G.-T., & Millero, F. J. (1979). Gradual increase of oceanic CO<sub>2</sub>. *Nature*, 277(5693), 205–206. <https://doi.org/10.1038/277205a0>
- Cheng, L., Trenberth, K. E., Gruber, N., Abraham, J. P., Fasullo, J. T., Li, G., et al. (2020). Improved estimates of changes in upper ocean salinity and the hydrological cycle. *American Meteorological Society Section: Journal of Climate*, 33(23), 10357–10381. <https://doi.org/10.1175/JCLI-D-20-0366.1>
- Clement, D., & Gruber, N. (2018). The eMLR(C\*) method to determine decadal changes in the global ocean storage of anthropogenic CO<sub>2</sub>. *Global Biogeochemical Cycles*, 32(4), 654–679. <https://doi.org/10.1002/2017GB005819>
- DeVries, T., Holzer, M., & Primeau, F. (2017). Recent increase in oceanic carbon uptake driven by weaker upper-ocean overturning. *Nature*, 542(7640), 215–218. <https://doi.org/10.1038/nature21068>
- Doney, S. C., Fabry, V. J., Feely, R. A., & Kleybas, J. A. (2009). Ocean acidification: The other CO<sub>2</sub> problem. *Annual Review of Marine Science*, 1(1), 169–192. <https://doi.org/10.1146/annurev.marine.010908.163834>

- Dong, Y., Bakker, D. C. E., Bell, T. G., Huang, B., Landschützer, P., Liss, P. S., & Yang, M. (2022). Update on the temperature corrections of global air-sea CO<sub>2</sub> flux estimates. *Global Biogeochemical Cycles*, 36(9), e2022GB007360. <https://doi.org/10.1029/2022GB007360>
- Dore, J. E., Lukas, R., Sadler, D. W., Church, M. J., & Karl, D. M. (2009). Physical and biogeochemical modulation of ocean acidification in the central North Pacific. *Proceedings of the National Academy of Sciences of the United States of America*, 106(30), 12235–12240. <https://doi.org/10.1073/pnas.0906044106>
- Etopo2 (2001). ETOPO2, global 2 Arc-minute ocean depth and land elevation from the US national geophysical data center (NGDC) [Dataset]. National Geophysical Data Center/NESDIS/NOAA/U.S. Department of Commerce. (Research Data Archive at the National Center for Atmospheric Research, Computational and Information Systems Laboratory). <https://doi.org/10.5065/D6668B75>
- Fay, A. R., Gregor, L., Landschützer, P., McKinley, G. A., Gruber, N., Gehlen, M., et al. (2021). SeaFlux: Harmonization of air–sea CO<sub>2</sub> fluxes from surface pCO<sub>2</sub> data products using a standardized approach. *Earth System Science Data*, 13(10), 4693–4710. <https://doi.org/10.5194/essd-13-4693-2021>
- Fay, A. R., & McKinley, G. A. (2013). Global trends in surface ocean pCO<sub>2</sub> from in situ data. *Global Biogeochemical Cycles*, 27(2), 541–557. <https://doi.org/10.1002/gbc.20051>
- Feely, R. A., Sabine, C. L., Lee, K., Berelson, W., Kleypas, J., Fabry, V. J., & Millero, F. J. (2004). Impact of anthropogenic CO<sub>2</sub> on the CaCO<sub>3</sub> system in the oceans. *Science*, 305(5682), 362–366. <https://doi.org/10.1126/science.1097329>
- Friedlingstein, P., Jones, M. W., O’Sullivan, M., Andrew, R. M., Bakker, D. C. E., Hauck, J., et al. (2022). Global carbon budget 2021. *Earth System Science Data*, 14(4), 1917–2005. <https://doi.org/10.5194/essd-14-1917-2022>
- Friis, K., Körtzinger, A., Pätsch, J., & Wallace, D. W. R. (2005). On the temporal increase of anthropogenic CO<sub>2</sub> in the subpolar North Atlantic. *Deep Sea Research Part I: Oceanographic Research Papers*, 52(5), 681–698. <https://doi.org/10.1016/j.dsr.2004.11.017>
- Friis, K., Körtzinger, A., & Wallace, D. W. R. (2003). The salinity normalization of marine inorganic carbon chemistry data. *Geophysical Research Letters*, 30(2), 1085. <https://doi.org/10.1029/2002GL015898>
- GlobalView-CO2 (2011). Cooperative atmospheric data integration project—Carbon dioxide [Dataset]. Retrieved from <https://gml.noaa.gov/ccgg/globalview/>
- Gloege, L., McKinley, G. A., Landschützer, P., Fay, A. R., Frölicher, T. L., Fyfe, J. C., et al. (2021). Quantifying errors in observationally based estimates of ocean carbon sink variability. *Global Biogeochemical Cycles*, 35(4), e2020GB006788. <https://doi.org/10.1029/2020GB006788>
- Gray, A. R., Johnson, K. S., Bushinsky, S. M., Riser, S. C., Russell, J. L., Talley, L. D., et al. (2018). Autonomous biogeochemical floats detect significant carbon dioxide outgassing in the high-latitude southern ocean. *Geophysical Research Letters*, 45(17), 9049–9057. <https://doi.org/10.1029/2018GL078013>
- Gregor, L., & Gruber, N. (2021). OceanSODA-ETHZ: A global gridded data set of the surface ocean carbonate system for seasonal to decadal studies of ocean acidification. *Earth System Science Data*, 13(2), 777–808. <https://doi.org/10.5194/essd-13-777-2021>
- Gregor, L., Kok, S., & Monteiro, P. M. S. (2017). Empirical methods for the estimation of southern ocean CO<sub>2</sub>: Support vector and random forest regression. *Biogeosciences*, 14(23), 5551–5569. <https://doi.org/10.5194/bg-14-5551-2017>
- Gruber, N. (1998). Anthropogenic CO<sub>2</sub> in the Atlantic Ocean. *Global Biogeochemical Cycles*, 12(1), 165–191. <https://doi.org/10.1029/97GB03658>
- Gruber, N., Bakker, D. C. E., DeVries, T., Gregor, L., Hauck, J., Landschützer, P., et al. (2023). Trends and variability in the ocean carbon sink. *Nature Reviews Earth & Environment*, 4(2), 119–134. <https://doi.org/10.1038/s43017-022-00381-x>
- Gruber, N., Clement, D., Carter, B. R., Feely, R. A., Heuven, S. V., Hoppema, M., et al. (2019). The oceanic sink for anthropogenic CO<sub>2</sub> from 1994 to 2007. *Science*, 363(6432), 1193–1199. <https://doi.org/10.1126/science.aau5153>
- Gruber, N., Gloor, M., Fletcher, S. E. M., Doney, S. C., Dutkiewicz, S., Follows, M. J., et al. (2009). Oceanic sources, sinks, and transport of atmospheric CO<sub>2</sub>. *Global Biogeochemical Cycles*, 23(1), GB1005. <https://doi.org/10.1029/2008GB003349>
- Gruber, N., Sarmiento, J. L., & Stocker, T. F. (1996). An improved method for detecting anthropogenic CO<sub>2</sub> in the oceans. *Global Biogeochemical Cycles*, 10(4), 809–837. <https://doi.org/10.1029/96GB01608>
- Hauck, J., Völker, C., Wang, T., Hoppema, M., Losch, M., & Wolf-Gladrow, D. A. (2013). Seasonally different carbon flux changes in the southern ocean in response to the southern annular mode. *Global Biogeochemical Cycles*, 27(4), 1236–1245. <https://doi.org/10.1002/2013GB004600>
- Hauck, J., Zeising, M., Le Quéré, C., Gruber, N., Bakker, D. C. E., Bopp, L., et al. (2020). Consistency and challenges in the ocean carbon sink estimate for the global carbon budget. *Frontiers in Marine Science*, 7, 852. <https://doi.org/10.3389/fmars.2020.571720>
- Ilyina, T., Six, K. D., Segsneider, J., Maier-Reimer, E., Li, H., & Núñez-Riboni, I. (2013). Global ocean biogeochemistry model HAMOCC: Model architecture and performance as component of the MPI-Earth system model in different CMIP5 experimental realizations. *Journal of Advances in Modeling Earth Systems*, 5(2), 287–315. <https://doi.org/10.1029/2012MS000178>
- IPCC. (2021). Climate change 2021: The physical science basis. In V. Masson-Delmotte, P. Zhai, A. Pirani, S. L. Connors, C. Péan, S. Berger, et al. (Eds.), *Contribution of Working Group I to the Sixth Assessment Report of the Intergovernmental Panel on Climate Change*. Cambridge University Press, Cambridge, United Kingdom and New York, NY, USA. <https://doi.org/10.1017/9781009157896>
- Jacobson, A. R., Mikaloff Fletcher, S. E., Gruber, N., Sarmiento, J. L., & Gloor, M. (2007). A joint atmosphere–ocean inversion for surface fluxes of carbon dioxide: 1. Methods and global-scale fluxes. *Global Biogeochemical Cycles*, 21(1), GB1019. <https://doi.org/10.1029/2005GB002556>
- Joos, F., Plattner, G.-K., Stocker, T. F., Marchal, O., & Schmittner, A. (1999). Global warming and marine carbon cycle feedbacks on future atmospheric CO<sub>2</sub>. *Science*, 284(5413), 464–467. <https://doi.org/10.1126/science.284.5413.464>
- Keeling, R. (2005). Comment on “The ocean sink for anthropogenic CO<sub>2</sub>”. *Science*, 308(5729), 1743c. <https://doi.org/10.1126/science.1109620>
- Kepler, L., & Landschützer, P. (2019). Regional wind variability modulates the southern ocean carbon sink. *Scientific Reports*, 9(1), 1–10. <https://doi.org/10.1038/s41598-019-43826-y>
- Kepler, L., Landschützer, P., Gruber, N., Lauvset, S. K., & Stemmler, I. (2020a). Mapped observation-based oceanic dissolved inorganic carbon (DIC), monthly climatology, from January to December (based on observations between 2004 and 2017), from the Max-Planck-Institute for Meteorology (MOBO-DIC\_mpim) [Dataset]. NOAA National Centers for Environmental Information, NCEI Accession 0221526. Retrieved from <https://www.nccei.noaa.gov/access/metadata/landing-page/bin/iso?id=gov.noaa.nodc%3A0221526>
- Kepler, L., Landschützer, P., Gruber, N., Lauvset, S. K., & Stemmler, I. (2020b). Seasonal carbon dynamics in the near-global ocean. *Global Biogeochemical Cycles*, 34(12), e2020GB006571. <https://doi.org/10.1029/2020GB006571>
- Kerr, R. A. (2000). A North Atlantic climate pacemaker for the centuries. *Science*, 288(5473), 1984–1985. <https://doi.org/10.1126/science.288.5473.1984>
- Key, R. M., Kozyr, A., Sabine, C. L., Lee, K., Wanninkhof, R., Bullister, J. L., et al. (2004). A global ocean carbon climatology: Results from global data analysis project (GLODAP). *Global Biogeochemical Cycles*, 18(4), GB4031. <https://doi.org/10.1029/2004GB002247>
- Lacroix, F., Ilyina, T., & Hartmann, J. (2020). Oceanic CO<sub>2</sub> outgassing and biological production hotspots induced by pre-industrial river loads of nutrients and carbon in a global modeling approach. *Biogeosciences*, 17(1), 55–88. <https://doi.org/10.5194/bg-17-55-2020>
- Landschützer, P., Gruber, N., & Bakker, D. C. E. (2016). Decadal variations and trends of the global ocean carbon sink. *Global Biogeochemical Cycles*, 30(10), 1396–1417. <https://doi.org/10.1002/2015GB005359>

- Landschützer, P., Gruber, N., Bakker, D. C. E., & Schuster, U. (2014). Recent variability of the global ocean carbon sink. *Global Biogeochemical Cycles*, 28(9), 927–949. <https://doi.org/10.1002/2014GB004853>
- Landschützer, P., Gruber, N., Bakker, D. C. E., Schuster, U., Nakaoka, S., Payne, M. R., et al. (2013). A neural network-based estimate of the seasonal to inter-annual variability of the Atlantic Ocean carbon sink. *Biogeosciences*, 10(11), 7793–7815. <https://doi.org/10.5194/bg-10-7793-2013>
- Landschützer, P., Gruber, N., Haumann, A., Rödenbeck, C., Bakker, D. C. E., van Heuven, S., et al. (2015). The reinvigoration of the southern ocean carbon sink. *Science*, 349(6253), 1221–1224. <https://doi.org/10.1126/science.aab2620>
- Landschützer, P., Keppler, L., & Ilyina, T. (2022). Chapter 13: Ocean systems. In *Balancing greenhouse gas budgets—Accounting for natural and anthropogenic flows of CO<sub>2</sub> and other trace gases* (1st ed.). Elsevier.
- Lauvset, S. K., Key, R. M., Olsen, A., van Heuven, S., Velo, A., Lin, X., et al. (2016). A new global interior ocean mapped climatology: The 1°×1° GLODAP version 2. *Earth System Science Data*, 8(2), 325–340. <https://doi.org/10.5194/essd-8-325-2016>
- Lauvset, S. K., Lange, N., Tanhua, T., Bittig, H. C., Olsen, A., Kozyr, A., et al. (2021). An updated version of the global interior ocean biogeochemical data product, GLODAPv2.2021. *Earth System Science Data*, 13(12), 5565–5589. <https://doi.org/10.5194/essd-13-5565-2021>
- Lenton, A., & Matear, R. J. (2007). Role of the southern annular mode (SAM) in southern ocean CO<sub>2</sub> uptake. *Global Biogeochemical Cycles*, 21(2), GB2016. <https://doi.org/10.1029/2006GB002714>
- Le Quéré, C., Rödenbeck, C., Buitenhuis, E. T., Conway, T. J., Langenfelds, R., Gomez, A., et al. (2007). Saturation of the southern ocean CO<sub>2</sub> sink due to recent climate change. *Science*, 316(5832), 1735–1738. <https://doi.org/10.1126/science.1136188>
- Lovenduski, N. S., Gruber, N., & Doney, S. C. (2008). Toward a mechanistic understanding of the decadal trends in the southern ocean carbon sink. *Global Biogeochemical Cycles*, 22(3), GB3016. <https://doi.org/10.1029/2007GB003139>
- Lovenduski, N. S., Gruber, N., Doney, S. C., & Lima, I. D. (2007). Enhanced CO<sub>2</sub> outgassing in the southern ocean from a positive phase of the southern annular mode. *Global Biogeochemical Cycles*, 21(2), GB2026. <https://doi.org/10.1029/2006GB002900>
- Mantua, N. J., & Hare, S. R. (2002). The Pacific decadal oscillation. *Journal of Oceanography*, 58(1), 35–44. <https://doi.org/10.1023/A:1015820616384>
- Matear, R. J., & Hirst, A. C. (1999). Climate change feedback on the future oceanic CO<sub>2</sub> uptake. *Tellus B: Chemical and Physical Meteorology*, 51(3), 722–733. <https://doi.org/10.3402/tellusb.v51i3.16472>
- Matsumoto, K., & Gruber, N. (2005). How accurate is the estimation of anthropogenic carbon in the ocean? An evaluation of the DeltaC\* method. *Global Biogeochemical Cycles*, 19(3), GB3014. <https://doi.org/10.1029/2004GB002397>
- Mauritsen, T., Bader, J., Becker, T., Behrens, J., Bittner, M., Brokopf, R., et al. (2019). Developments in the MPI-M Earth system model version 1.2 (MPI-ESM1.2) and its response to increasing CO<sub>2</sub>. *Journal of Advances in Modeling Earth Systems*, 11(4), 998–1038. <https://doi.org/10.1029/2018MS001400>
- McKinley, G. A., Fay, A. R., Eddelbar, Y. A., Gloege, L., & Lovenduski, N. S. (2020). External forcing explains recent decadal variability of the ocean carbon sink. *AGU Advances*, 1(2), e2019AV000149. <https://doi.org/10.1029/2019AV000149>
- McNeil, B. I., & Matear, R. J. (2013). The non-steady state oceanic CO<sub>2</sub> signal: Its importance, magnitude and a novel way to detect it. *Biogeosciences*, 10(4), 2219–2228. <https://doi.org/10.5194/bg-10-2219-2013>
- McNeil, B. I., & Sasse, T. P. (2016). Future ocean hypercapnia driven by anthropogenic amplification of the natural CO<sub>2</sub> cycle. *Nature*, 529(7586), 383–386. <https://doi.org/10.1038/nature16156>
- Mikaloff Fletcher, S. E. M., Gruber, N., Jacobson, A. R., Doney, S. C., Dutkiewicz, S., Gerber, M., et al. (2006). Inverse estimates of anthropogenic CO<sub>2</sub> uptake, transport, and storage by the ocean. *Global Biogeochemical Cycles*, 20(2), GB2002. <https://doi.org/10.1029/2005GB002530>
- Olsen, A., Key, R. M., Heuven, S. V., Lauvset, S. K., Velo, A., Lin, X., et al. (2016). The global ocean data analysis project version 2 (GLODAPv2)—An internally consistent data product for the world ocean. *Earth System Science Data*, 8(2), 297–323. <https://doi.org/10.5194/essd-8-297-2016>
- Orr, J. C., Fabry, V. J., Aumont, O., Bopp, L., Doney, S. C., Feely, R. A., et al. (2005). Anthropogenic ocean acidification over the twenty-first century and its impact on calcifying organisms. *Nature*, 437(7059), 681–686. <https://doi.org/10.1038/nature04095>
- Regnier, P., Resplandy, L., Najjar, R. G., & Ciais, P. (2022). The land-to-ocean loops of the global carbon cycle. *Nature*, 603(7901), 401–410. <https://doi.org/10.1038/s41586-021-04339-9>
- Resplandy, L., Keeling, R. F., Rödenbeck, C., Stephens, B. B., Khattiwala, S., Rodgers, K. B., et al. (2018). Revision of global carbon fluxes based on a reassessment of oceanic and riverine carbon transport. *Nature Geoscience*, 1(7), 504–509. <https://doi.org/10.1038/s41561-018-0151-3>
- Rödenbeck, C., Bakker, D. C. E., Gruber, N., Iida, Y., Jacobson, A. R., Jones, S., et al. (2015). Data-based estimates of the ocean carbon sink variability—First results of the surface ocean pCO<sub>2</sub> Mapping intercomparison (SOCOM). *Biogeosciences*, 12(23), 7251–7278. <https://doi.org/10.5194/bg-12-7251-2015>
- Roemmich, D., & Gilson, J. (2009). The 2004–2008 mean and annual cycle of temperature, salinity, and steric height in the global ocean from the Argo Program. *Progress in Oceanography*, 52(2), 81–100. <https://doi.org/10.1016/j.poccean.2009.03.004>
- Roobaert, A., Laruelle, G. G., Landschützer, P., Gruber, N., Chou, L., & Regnier, P. (2019). The spatiotemporal dynamics of the sources and sinks of CO<sub>2</sub> in the global coastal ocean. *Global Biogeochemical Cycles*, 33(12), 1693–1714. <https://doi.org/10.1029/2019GB006239>
- Sabine, C. L., Feely, R. A., Gruber, N., Key, R. M., Lee, K., Bullister, J. L., et al. (2004). The oceanic sink for anthropogenic CO<sub>2</sub>. *Science*, 305(5682), 367–371. <https://doi.org/10.1126/science.1097403>
- Sabine, C. L., & Gruber, N. (2005). Response to comment on “The ocean sink for anthropogenic CO<sub>2</sub>”. *Science*, 308(5729), 1743. <https://doi.org/10.1126/science.1109949>
- Sabine, C. L., Key, R. M., Johnson, K. M., Millero, F. J., Poisson, A., Sarmiento, J. L., et al. (1999). Anthropogenic CO<sub>2</sub> inventory of the Indian Ocean. *Global Biogeochemical Cycles*, 13(1), 179–198. <https://doi.org/10.1029/1998GB900022>
- Sarmiento, J. L., & Gruber, N. (2002). Sinks for anthropogenic carbon. *Physics Today*, 55(8), 30–36. <https://doi.org/10.1063/1.1510279>
- Sarmiento, J. L., & Gruber, N. (2006). Carbon cycle, CO<sub>2</sub>, and climate: the anthropogenic perturbation. In *Ocean biogeochemical dynamics* (pp. 399–417). Princeton University Press.
- Sarmiento, J. L., Hughes, T. M. C., Stouffer, R. J., & Manabe, S. (1998). Simulated response of the ocean carbon cycle to anthropogenic climate warming. *Nature*, 393(6682), 245–249. <https://doi.org/10.1038/30455>
- Sarmiento, J. L., Le Quéré, C., & Pacala, S. W. (1995). Limiting future atmospheric carbon dioxide. *Global Biogeochemical Cycles*, 9(1), 121–137. <https://doi.org/10.1029/94GB01779>
- Sarmiento, J. L., & Sundquist, E. T. (1992). Revised budget for the oceanic uptake of anthropogenic carbon dioxide. *Nature*, 356(6370), 589–593. <https://doi.org/10.1038/356589a0>
- Sasse, T. P., McNeil, B. I., & Abramowitz, G. (2013). A novel method for diagnosing seasonal to inter-annual surface ocean carbon dynamics from bottle data using neural networks. *Biogeosciences*, 10(6), 4319–4340. <https://doi.org/10.5194/bg-10-4319-2013>

- Sharp, J. D., Fassbender, A. J., Carter, B. R., Johnson, G. C., Schultz, C., & Dunne, J. P. (2022). GOBAI-O<sub>2</sub>: Temporally and spatially resolved fields of ocean interior dissolved oxygen over nearly two decades. *Earth System Science Data Discussions*, 1–46. <https://doi.org/10.5194/essd-2022-308>
- Talley, L., Feely, R., Sloyan, B., Wanninkhof, R., Baringer, M., Bullister, J., et al. (2016). Changes in ocean heat, carbon content, and ventilation: A review of the first decade of GO-SHIP global repeat hydrography. *Annual Review of Marine Science*, 8(1), 185–215. <https://doi.org/10.1146/annurev-marine-052915-100829>
- Talley, L., Rosso, I., Kamenkovich, I., Mazloff, M. R., Wang, J., Boss, E., et al. (2019). Southern ocean biogeochemical float deployment strategy, with example from the Greenwich Meridian Line (GO-SHIP A12). *Journal of Geophysical Research: Oceans*, 124(1), 403–431. <https://doi.org/10.1029/2018JC014059>
- Tanhua, T., Körtzinger, A., Friis, K., Waugh, D. W., & Wallace, D. W. R. (2007). An estimate of anthropogenic CO<sub>2</sub> inventory from decadal changes in oceanic carbon content. *Proceedings of the National Academy of Sciences of the United States of America*, 104(9), 3037–3042. <https://doi.org/10.1073/pnas.0606574104>
- Terhaar, J., Frölicher, T. L., & Joos, F. (2022). Observation-constrained estimates of the global ocean carbon sink from Earth system models. *Biogeosciences Discussions*, 1–49. <https://doi.org/10.5194/bg-2022-134>
- Torres, O., Kwiatkowski, L., Sutton, A. J., Dorey, N., & Orr, J. C. (2021). Characterizing mean and extreme diurnal variability of ocean CO<sub>2</sub> system variables across marine environments. *Geophysical Research Letters*, 48(5), e2020GL090228. <https://doi.org/10.1029/2020GL090228>
- Turner, K. E., Smith, D. M., Katavouta, A., & Williams, R. G. (2022). Reconstructing ocean carbon storage with CMIP6 models and synthetic Argo observations. *Biogeosciences Discussions*, 1–29. <https://doi.org/10.5194/bg-2022-166>
- van Heuven, S., Pierrot, D., Rae, J., Lewis, E., & Wallace, D. (2011). *MATLAB program developed for CO<sub>2</sub> system calculations*. Oak Ridge, Tennessee: ORNL/CDIAC-105b. Carbon Dioxide Information Analysis Center, Oak Ridge National Laboratory, U.S. Department of Energy.
- Wallace, D. W. (1995). Monitoring global ocean carbon inventories. In *Scientific design for the common module of the global ocean observing system and the global climate observing system: An ocean observing system for climate: Final report of the ocean observing system development panel*. Texas A&M University.
- Wanninkhof, R., Asher, W. E., Ho, D. T., Sweeney, C., & McGillis, W. R. (2009). Advances in quantifying air-sea gas exchange and environmental forcing. *Annual Review of Marine Science*, 1(1), 213–244. <https://doi.org/10.1146/annurev.marine.010908.163742>
- Wanninkhof, R., Doney, S. C., Bullister, J. L., Levine, N. M., Warner, M., & Gruber, N. (2010). Detecting anthropogenic CO<sub>2</sub> changes in the interior Atlantic Ocean between 1989 and 2005. *Journal of Geophysical Research*, 115(C11), C11028. <https://doi.org/10.1029/2010JC006251>
- Watson, A. J., Schuster, U., Shutler, J. D., Holding, T., Ashton, I. G. C., Landschützer, P., et al. (2020). Revised estimates of ocean-atmosphere CO<sub>2</sub> flux are consistent with ocean carbon inventory. *Nature Communications*, 11(1), 4422. <https://doi.org/10.1038/s41467-020-18203-3>
- Wolter, K., & Timlin, M. S. (2011). El Niño/Southern Oscillation behaviour since 1871 as diagnosed in an extended multivariate ENSO index (MEI<sub>ext</sub>). *International Journal of Climatology*, 31(7), 1074–1087. <https://doi.org/10.1002/joc.2336>
- Zickfeld, K., Fyfe, J. C., Saenko, O. A., Eby, M., & Weaver, A. J. (2007). Response of the global carbon cycle to human-induced changes in southern hemisphere winds. *Geophysical Research Letters*, 34(12), L12712. <https://doi.org/10.1029/2006GL028797>